

# The Atmospheric Radiative Transfer Simulator ARTS, Version 2.6 — Deep Python Integration

Stefan A. Buehler<sup>a</sup>, Richard Larsson<sup>a</sup>, Oliver Lemke<sup>a</sup>, Simon  
Pfreundschuh<sup>b</sup>, Manfred Brath<sup>a</sup>, Ian Adams<sup>c</sup>, Stuart Fox<sup>d</sup>, Florian E.  
Roemer<sup>a</sup>, Paulina Czarnecki<sup>e</sup>, Patrick Eriksson<sup>b</sup>

<sup>a</sup>*Meteorological Institute, Center for Earth System Research and Sustainability (CEN),  
Universität Hamburg, Hamburg, Germany*

<sup>b</sup>*Department of Space, Earth and Environment, Chalmers University of  
Technology, Gothenburg, Sweden*

<sup>c</sup>*Mesoscale Atmospheric Processes Laboratory, NASA Goddard Space Flight  
Center, Greenbelt, Maryland, United States*

<sup>d</sup>*Met Office, FitzRoy Road, Exeter, EX1 3PB, UK*

<sup>e</sup>*Columbia University, New York, New York, United States*

---

## Abstract

The atmospheric radiative transfer simulator ARTS is a software for computing atmospheric absorption, scattering, the transfer of radiation through an atmosphere, and sensor characteristics. It is written in C++ and can simulate remote sensing observations and radiative energy fluxes. The article describes version 2.6 of the software. There are numerous changes compared to the last ARTS publication, the most striking being that the program is now controlled by Python scripts, which is convenient and allows for great flexibility. The article discusses the ARTS history, the theory behind the computations of absorption and radiative transfer, available solvers for atmospheres with scattering, the computation of energy fluxes and heating rates, and the built-in system for inverting remote observations to atmospheric state variables by optimal estimation. ARTS is publicly available, open source, and free of charge.

**Keywords:** atmospheric radiative transfer simulator, ARTS, infrared, microwave, radiation, absorption, scattering, spectroscopy, polarization, radiative transfer

**PACS:** 42.68.Ay, 42.68.Ca, 42.68.Ge, 42.68.Mj

---

*Preprint submitted to Journal of Quantitative Spectroscopy and Radiative Transfer April 29, 2024*

## 1. Introduction

### 1.1. Basics

The Atmospheric Radiative Transfer Simulator ARTS is a software, written primarily in C++, for calculating atmospheric absorption and scattering, and for simulating the transfer of radiation through planetary atmospheres. Philosophically, what sets it apart from other such programs is its very wide scope and its flexibility, unmatched by any other software that the authors are aware of.

ARTS can do radiative transfer simulations in 1D, 2D, and 3D spherical atmospheres, spherical geometry being a key feature for simulating limb observations. It is used for simulating remote sensing observations and retrieval, but also to compute radiative fluxes and heating rates as a reference for faster radiation schemes in atmospheric circulation models for climate research and weather forecasting.

The radiative transfer is fully polarised, allowing simulation of up to four Stokes components, which is important for simulating sensors with polarisation capabilities, and even sometimes for correctly simulating simple polarisation sensors observing at frequencies where the radiation is polarised, for example by Zeeman splitting.

ARTS also does analytical or semi-analytical Jacobians (derivatives of the simulated observation with respect to changes in atmospheric state or model parameters), and these can be used in a built-in optimal estimation method (OEM) implementation for atmospheric state retrieval.

A significant part of ARTS deals with the calculation of absorption spectra from line-by-line spectroscopic data catalogues. In line with the overall philosophy, also this part is very flexible, allowing for example calculations with broadening gases other than air, to the extent that broadening parameters are available. This is important for simulating radiation on other planets.

Additionally, other types of absorption can be added, including predefined continua, measured absorption cross-sections, and collision-induced absorption spectra.

For simulations with scattering, a number of different scattering solvers are available, including a native scheme based on lambda-iteration (DOIT), a native Monte-Carlo scheme, and also well-known schemes such as DISORT. There also is a sophisticated system for specifying the single scattering properties that are needed for these simulations.

## 1.2. History

Historically, ARTS started in 2000 as a collaboration between Patrick Eriksson (Chalmers) and Stefan Buehler (then University of Bremen). The program was open source from the start and many others have made important contributions over the years.

Important early milestones were the addition of water vapor continuum absorption by Thomas Kuhn [1] and the iterative scattering solver by Claudia Emde and Sreerekha T. R. [2, 3]. Eriksson et al. [4] describes the first OEM implementation (in Matlab) and Buehler et al. [5] gives the first ARTS overview.

Cory Davis [6] added a Monte Carlo scattering solver and Christian Melsheimer [7] did a first validation and intercomparison with other radiative transfer models. Buehler et al. [8] describes the first application of ARTS for radiative flux and cooling rate calculations, and Eriksson et al. [9] developed the matrix sensor representation that is still in use today. Buehler et al. [10] developed a method to represent integral radiation quantities by a few representative frequencies, Buehler et al. [11] describes the handling of absorption in lookup tables, and Eriksson et al. [12] is the second ARTS overview paper.

In 2014, Richard Larsson added code to handle Zeeman splitting [13, 14]. This code was revised over the years and Zeeman splitting coefficients were updated for oxygen and other species [15, 16].

For calculations with ice particle scattering, dedicated databases of single scattering data for different particle shapes and sizes were developed for ARTS for both randomly oriented [17] and oriented [18] particles. Very recently, polynomial fits to HITRAN absorption cross-section data [19] were developed to allow simulations with a large number of halocarbon species [20].

In general, ARTS release versions have an even last digit, development versions an odd last digit. The most recent ARTS overview paper was [21], describing Version 2.2, and this article is about Version 2.6. The most user-visible change between these versions is the Python integration, but there also have been numerous other improvements, such as a new core to calculate atmospheric absorption, updates to the clear-sky radiative transfer core, new scattering solvers, and the capability to do optimal estimation retrievals inside ARTS. These changes are described in subsequent sections.

### 74 1.3. ARTS use — literature analysis

75 It is interesting to see for what applications ARTS is used in practice.  
76 For this, we did a search on Web of Science for all articles that cite one of  
77 the three primary ARTS papers [21, 12, 5], between 2018 and June 2023.  
78 This yielded 133 publications. Out of these, 29 just mention the program.  
79 Often they are about other radiative transfer software (for example [22, 23])  
80 or spectroscopy (for example [24, 25]).

81 The remaining 104 publications actually used ARTS for their work. The  
82 largest group of these (52 publications) deals with remote sensing of the  
83 clear atmosphere (without scattering in the radiative transfer setup). Out  
84 of these, many used ground-based microwave radiometers for profiles of at-  
85 mospheric trace gases and temperature. Examples include tropospheric wa-  
86 ter [26], stratospheric and mesospheric water [27, 28, 29, 30], stratospheric  
87 and mesospheric ozone [31, 32, 33, 34, 35], mesospheric carbon monoxide  
88 [36, 37, 38], temperature [39, 40], and wind [41, 38].

89 Another significant group, still within the clear-sky category, are publi-  
90 cations with existing or planned satellite sensors, with examples including  
91 operational meteorological microwave and infrared sounders [42, 43, 44, 45,  
92 46, 47, 48, 49, 20] and microwave to infrared limb sounders [50, 51, 52, 53, 54,  
93 55, 56, 16]. In addition to these, yet another interesting clear-sky application  
94 is the retrieval of the rotational temperature from stratospheric and lower  
95 thermospheric O<sub>2</sub> airglow emissions [57, 58].

96 The other big group of publications that used ARTS (37 publications out  
97 of 104) deals with all-sky observations of the atmosphere and/or the retrieval  
98 of hydrometeor properties, so they require radiative transfer simulations with  
99 scattering. Applications here include passive microwave to sub-mm wave  
100 sensors, radars, and their synergy [59, 60, 61, 62, 63, 64, 65, 66, 67, 68, 69,  
101 70, 71, 72, 73, 74]. Many are in preparation of the upcoming Ice Cloud  
102 Imager (ICI) mission on Metop Second Generation [75, 76, 77, 78]. Also,  
103 several focus specifically on polarised observations [17, 79, 18, 80]. Other  
104 studies focus on terahertz sensors [81, 82, 83, 84, 85] or on infrared sensors  
105 [86].

106 A growing application area is the simulation of atmospheric infrared en-  
107 ergy fluxes and associated heating rates in the context of climate modeling  
108 [20, 87, 88, 89, 90]. Although ARTS so far was not capable of simulating  
109 radiative transfer in the solar part of the spectrum, a few studies used its ca-  
110 pability to compute atmospheric absorption at these frequencies [91, 92, 93].

111 The overwhelming majority of use is for Earth, but there are also reported  
112 applications for Venus [94] and Mars [95]. Also, while the overwhelming  
113 majority of studies is in the context of atmospheric science, there is reported  
114 use for retrieving surface temperature [96, 97].

115 In summary, ARTS has been used for a wide range of applications. The  
116 vast majority are remote sensing applications, with atmospheric energetics  
117 picking up in recent years. Applications with and without scattering are  
118 almost equally frequent, with a slight majority for clear-sky. A big majority  
119 of applications is passive, but radar also plays a certain role [62, 69, 60].

120 In terms of frequency region, microwave to sub-mm applications were  
121 most common, terahertz and infrared applications were less frequent, and  
122 solar applications rare (as expected). This distribution aligns well with the  
123 historical development of ARTS, which started as a microwave program and  
124 over the years expanded to higher and higher frequencies.

#### 125 1.4. *Python integration*

126 In order to allow the widest possible range of different absorption and  
127 radiative transfer simulations, ARTS uses the concept of workspace variables  
128 (which hold quantities of interest, such as a vector of simulation frequencies)  
129 and workspace methods (which operate on the workspace variables to for  
130 example calculate absorption). In the past, calculations were specified in  
131 ARTS' own – quite primitive – scripting language. This is still possible,  
132 but for most users it will be much more convenient to use pyarts, the new  
133 Python interface to these workspace variables and methods, and thus specify  
134 the calculation in the form of a Python script.

135 It is worth to point out here, that pyarts and ARTS really are the same  
136 program. Pyarts just is the name of the Python module. To work with arts  
137 in Python, the user has to import module pyarts and create an object of type  
138 Workspace. Workspace variables and methods are simply member variables  
139 and member functions of that object. For explicit examples see the ARTS  
140 online documentation, in particular 'getting started' there. The location is  
141 given in Section 'Obtaining ARTS' at the end of this article.

142 Just enter the name of a workspace variable in an interactive Python  
143 session to see its content, or use Python's print() function. In some cases,  
144 you may have to append '.value' after the variable name to access its contents.  
145 In the ipython shell, type a question mark at the end of a workspace methods  
146 or variable name to see its built-in documentation.

147 An overall design goal for pyarts was that it should feel ‘pythonic’ —  
 148 natural for any user familiar with other python packages. The interface uses  
 149 the pybind11 C++ header library for translation from C++ to python [98].  
 150 Pyarts allows all computations that the traditional interface allowed, but  
 151 with much greater convenience and flexibility. We therefore recommend to  
 152 use this new interface, even though the old one is still maintained for now (it  
 153 may be phased out at some point in the future). To ease the transition, we  
 154 provide also a simple method that parses traditional ARTS controlfiles and  
 155 translates them into python.

## 156 2. Radiative transfer

### 157 2.1. Theory

The core equation for ARTS’ internal radiative transfer solver is the vector Schwarzschild equation

$$\frac{d\vec{I}}{ds} = -\mathbf{K} (\vec{I} - \vec{J}) \quad (1)$$

158 where  $\vec{I}$  is the four component Stokes vector,  $\vec{J}$  is the source term, and  $\mathbf{K}$  is  
 159 the propagation matrix, which describes how the radiation is modified along  
 160 an infinitesimal path distance  $ds$ .

161 The equation formally looks exactly as the original scalar Schwarzschild  
 162 equation [99], but has a wider scope, not only because  $\mathbf{K}$  is a matrix and  $\vec{I}$   
 163 and  $\vec{J}$  are vectors, but also because  $\mathbf{K}$  and  $\vec{J}$  include the effect of scattering,  
 164 whereas Schwarzschild thought only about absorption and thermal emission.  
 165 The advantage of casting the radiative transfer differential equation in this  
 166 form is that its integral form is known.

167 One key implementation difference of ARTS version 2.6 compared to ver-  
 168 sion 2.2 is that it now uses a dedicated data type for the propagation matrix  
 169  $\mathbf{K}$ , which greatly speeds up the calculation of polarized radiative transfer by  
 170 simplifying both matrix inversions and matrix exponential calculations.

We assume in ARTS and in this subsection that  $\mathbf{K}$  and  $\vec{J}$  are approxi-  
 mately constant over a small enough distance  $r = |s_{i+1} - s_i|$ , where  $i$  is some  
 discrete positional index. In fact, we discretize ARTS in a level-by-level man-  
 ner and both  $\mathbf{K}$  and  $\vec{J}$  are simply the average of the surrounding levels when a  
 layer is constructed, explicitly,  $\mathbf{K} = (\mathbf{K}_i + \mathbf{K}_{i+1}) / 2$  and  $\vec{J} = (\vec{J}_i + \vec{J}_{i+1}) / 2$ .  
 Given this, the transmission through the atmosphere between two positions

can be written as

$$\vec{I}_{i+1} = \exp(-\mathbf{K}r) \vec{I}_i \quad (2)$$

when the source term is negligibly small, or

$$\vec{I}_{i+1} = \exp(-\mathbf{K}r) (\vec{I}_i - \vec{J}) + \vec{J} \quad (3)$$

171 when the source term must be taken into account.

172 The propagation matrix has in other places been called the extinction  
173 matrix or the attenuation matrix. We prefer the term propagation matrix,  
174 because this matrix also deals with the effect of Faraday rotation, which  
175 just moves energy between different polarization states (higher Stokes com-  
176 ponents), but does not decrease the total intensity (first Stokes component),  
177 so that  $\mathbf{K}$  is not always associated with extinction. The physical unit of  $\mathbf{K}$   
178 is  $\text{m}^{-1}$ .

There are only 7 independent variables in the  $4 \times 4$  propagation matrix

$$\mathbf{K} = \begin{bmatrix} A & B & C & D \\ B & A & U & V \\ C & -U & A & W \\ D & -V & -W & A \end{bmatrix}, \quad (4)$$

179 so only these are kept. The Zeeman effect needs to make use of all seven  
180 components, Faraday rotation only makes use of the  $U$ -component, and all  
181 the other line-by-line, continua, and collision-induced-absorption models of  
182 ARTS only make use of the  $A$ -component, corresponding to the scalar ex-  
183 tinction coefficient for unpolarized radiation, which would be the sum of  
184 absorption coefficient and scattering coefficient.

The matrix exponential  $\exp(-\mathbf{K}r)$  is computed after a rewrite as

$$\exp(-Ar) \exp(\mathbf{K}'), \quad (5)$$

where  $\mathbf{K}'$  is as Equation 4 but with  $A = 0$  and scaled already by  $r$  [this is the same solution here as found in 100]. We can rewrite the remaining matrix exponential using the Cayley-Hamilton theorem as

$$\exp(\mathbf{K}') = c_0 \mathbf{I} + c_1 \mathbf{K}' + c_2 \mathbf{K}'^2 + c_3 \mathbf{K}'^3, \quad (6)$$

where  $c_0$ - $c_3$  are four coefficients that can be found using eigenvalue decomposition. The eigenvalues ( $\lambda$ ) are found from solving the characteristic polynomial,

$$\begin{aligned} 0 &= \lambda^4 + b\lambda^2 + c \\ b &= U^2 + V^2 + W^2 - B^2 - C^2 - D^2 \\ c &= -(DU - CV + BW)^2 \\ s &= \sqrt{b^2 - 4c} \\ x^2 &= \sqrt{\frac{s-b}{2}} \\ y^2 &= \sqrt{\frac{s+b}{2}}, \end{aligned} \quad (7)$$

where  $x^2$  and  $y^2$  are the positive and negative parts of the solutions for  $\lambda^2$ , respectively, as their practical real values. The coefficients of Equation 6 are found from the set of equations

$$\begin{aligned} e^x &= c_0 + c_1x + c_2x^2 + c_3x^3 \\ e^{-x} &= c_0 - c_1x + c_2x^2 - c_3x^3 \\ e^{iy} &= c_0 + ic_1y - c_2y^2 - ic_3y^3 \\ e^{-iy} &= c_0 - ic_1y - c_2y^2 + ic_3y^3, \end{aligned} \quad (8)$$

which yields

$$c_0 = \frac{x^2 \cos y + y^2 \cosh x}{x^2 + y^2} \quad (9)$$

$$c_1 = \frac{x^2 \frac{\sin y}{y} + y^2 \frac{\sinh x}{x}}{x^2 + y^2} \quad (10)$$

$$c_2 = \frac{\cosh x - \cos y}{x^2 + y^2} \quad (11)$$

$$c_3 = \frac{\frac{\sinh x}{x} - \frac{\sin y}{y}}{x^2 + y^2}. \quad (12)$$

Lastly, it is important to keep some limits in mind as  $x \rightarrow 0$  or  $y \rightarrow 0$  as the hyperbolic and the trigonometric functions are not computationally stable while they are divided by some numbers close to 0. For convenience, these



limits are

$$\begin{aligned}
c_0 : \quad \lim_{x \rightarrow 0} c_0 &= \lim_{y \rightarrow 0} c_0 &= 1 \\
c_1 : \quad \lim_{x \rightarrow 0} c_1 &= \lim_{y \rightarrow 0} c_1 &= 1 \\
c_2 : \quad \lim_{x \rightarrow 0 \wedge y \rightarrow 0} c_2 &= \frac{1}{2} \\
c_3 : \quad \lim_{x \rightarrow 0 \wedge y \rightarrow 0} c_3 &= \frac{1}{6} \\
\vee \quad \lim_{x \rightarrow 0} c_3 &= \frac{1}{y^2} - \frac{\sin y}{y^3} \\
\vee \quad \lim_{y \rightarrow 0} c_3 &= \frac{\sinh x}{x^3} - \frac{1}{x^2}.
\end{aligned} \tag{13}$$

185 We have opted for a value of 0.001 as a limit of actual 0 of  $x$  and  $y$ . As  
186 a comment on the numerics of this matrix exponential solution, we are not  
187 sure how stable the method really is. The work by Moler and Van Loan [101]  
188 gives the scaling and squaring method with the Padé approximation as one  
189 of the most effective algorithms at hand. The algorithm above is more than  
190 an order of magnitude faster in our experience. The differences between the  
191 methods in computed results are also small if the maximum value in  $\mathbf{K}'$  is  
192 small (less than 0.1) but grow out of control if this is large (above 10). We  
193 cannot judge which method is then better, but we do note that the Padé  
194 approximation algorithm tends to return infinities when the algorithm above  
195 still returns large but finite values. In any case, since an atmospheric layer  
196 with too much absorption is a poorly designed atmospheric layer, for the sake  
197 of radiative transfer using the faster algorithm above is simply better.

The source function is first computed as

$$\vec{J} = \mathbf{K}^{-1} \left( \vec{\alpha} B_P + \vec{J}_n + \vec{J}_s + \vec{J}_\odot \right), \tag{14}$$

198 where  $\vec{\alpha} = \{A, B, C, D\}^\top$  is the absorption vector,  $B_P$  is Planck's function  $\vec{J}_n$   
199 is the emission correction due to non-local thermodynamic equilibrium,  $\vec{J}_s$   
200 is the additional particulate scattering source term, and  $\vec{J}_\odot$  is the additional  
201 solar scattering term. When the atmosphere is in local thermodynamic equi-  
202 librium, and there is no sun, and scattering is not considered, this simply  
203 translates to  $\vec{J} = \{B_P, 0, 0, 0\}^\top$ . This can be seen from noting that  $\mathbf{K}^{-1}\mathbf{K}$   
204 is the unit matrix and  $\vec{\alpha}$  is just the first column of  $\mathbf{K}$ . The  $\vec{J}_n$  is computed  
205 as the additional emission caused by non-local thermodynamic equilibrium  
206 added up for every absorption species. Note also that the split above is done  
207 mostly for pedagogical reasons. Inside ARTS  $\vec{J}_n$  and  $\vec{J}_s$  are treated as the  
208 same variable, but  $\vec{J}_\odot$  is still treated separately.

209 The background source term,  $\vec{I}_0$ , depends on the background of the prop-  
 210 agation path. Three such backgrounds are allowed: (1) surface, (2) space,  
 211 and (3) a cloud box. The surface in particular might itself recursively spawn  
 212 a new set of radiative transfer calculations to compute the incoming radia-  
 213 tion. Note that the sun is not a possible background, since its input radiation  
 214 is implied by the geometry of the problem.

## 215 2.2. Simulations with a solar source term

In this subsection we will give a brief overview about simulations with a solar source. There will be also an upcoming article dedicated to this. The simulation of solar radiation in ARTS is based on the assumption that the distance between the sun and the top of the atmosphere (TOA) of the planet is much larger than the radius of the sun. In that case, the incoming spectral radiance in direction  $\Omega$  at top of the atmosphere is assumed to be parallel (collimated beam approximation, [102]) and can be described as

$$I_{s,TOA}(\Omega) = F_s \sin^2 \alpha \cdot \delta(\Omega - \Omega') \quad (15)$$

216 with  $\Omega'$  the direction from the sun to TOA,  $\alpha$  the solar angular radius at  
 217 TOA and  $F_s$  the solar spectral irradiance at the position of the sun. As  
 218 ARTS assumes a spherical geometry  $\Omega'$  and  $\alpha$  depend on the geographical  
 219 position. In addition to the irradiance spectrum a solar source is defined by  
 220 the radius of the sun, its distance to the planet and the geographical position  
 221 where sun is at zenith on the planet. A solar spectrum can be defined by a  
 222 black body with an effective emission temperature or with an arbitrary user-  
 223 defined spectrum. There are two solvers in ARTS capable of simulations with  
 224 a solar source term:

225 First, there is ARTS' internal clear-sky solver *iyClearsky*. It is a 3D fully  
 226 polarized radiative transfer solver for spherical geometry. It includes first  
 227 order molecular scattering from solar sources but no scattering of particulates  
 228 or scattering from thermal sources.

229 Second, there is CDISORT [103], which is DISORT 2.1 [102] ported to  
 230 C and for simplicity called DISORT from here on. It is a 1D non-polarized  
 231 radiative transfer solver for plane parallel atmospheres and can handle multi-  
 232 ple scattering. In contrast to *iyClearsky*, DISORT it can have only one solar  
 233 source. As DISORT is a plane parallel solver and ARTS assumes a spherical  
 234 geometry, it needs to be run for a specific geographic position because the  
 235 local solar zenith angle, which DISORT internally needs, is calculated from

the specific geographic position and the geographic zenith position of the sun.

For both solvers molecular scattering (Rayleigh scattering) is provided by a parametrization from M. Callan, University of Colorado [102] based on the results of Bates [104] for the scattering cross sections and the Rayleigh phase matrix including depolarization from Hansen et al. [105].

### 3. Absorption

#### 3.1. Computing absorption from spectroscopic data

How ARTS computes absorption coefficients by summing up spectral lines based on spectroscopic data has been completely re-implemented. The set of operators and multiplications for each spectral line is

$$\alpha = (1 + G_{lm} - iY_{lm}) S(T, p, \dots) N(\nu, \dots) F(\nu, \dots), \quad (16)$$

where  $\alpha$  is the complex absorption coefficient, whose real part is the attenuation and imaginary part is the dispersion. The  $G_{lm}$  and  $Y_{lm}$  parameters are the second and first order line mixing coefficients, the  $S$  operator computes the line strength, the  $N$  operator renormalizes the line shape, and the  $F$  operator computes the line shape.

There are too many variants and combinations of these operators available to go over all of them here. As one example, the adaptation of default HITRAN line-by-line data for ARTS [24, as found online using just their par-parameters 2023-08-23] uses

$$\alpha = \frac{x_i p}{kT} S_i \frac{Q(T_i)}{Q(T)} \exp\left(E_i \frac{T - T_i}{kT T_i}\right) \frac{\nu (\exp[h\nu/kT] - 1)}{\nu_i (\exp[h\nu_i/kT_i] - 1)} F_v(\dots), \quad (17)$$

where the terms before the  $F_v(\dots)$  line profile operator represent the  $S$  and  $N$  operations of Equation 16,  $x_i$  is the volume mixing ratio of the molecule in question,  $p$  is pressure,  $k$  is Boltzmann's constant,  $T$  is temperature,  $S_i$  is the reference line strength of the absorption line as provided by HITRAN,  $Q$  is the total internal partition sum operator for some temperature [106],  $T_i$  is the reference temperature of the line (for HITRAN always 296 K),  $E_i$  is the HITRAN lower state energy level of the absorption line,  $\nu$  is the frequency at which absorption is sampled,  $\nu_i$  is the HITRAN reference line center of the absorption line, and  $h$  is the Planck constant. HITRAN does not provide any

line mixing parameters by default, so the  $1 + G_{lm} - iY_{lm}$  term of Equation 16 disappears completely.

The  $F_v(\dots)$  line profile operator in this example case is

$$F_v(\dots) = \frac{1}{\sqrt{\pi}G_D} w\left(\frac{\nu - \nu_i - \Delta\nu_{0,i} + G_{0,i}}{G_D}\right) \quad (18)$$

$$G_D = \frac{\nu_i}{c} \sqrt{\frac{2000RT}{m_i}} \quad (19)$$

$$G_{0,i} = x_i g_{0,i,s} p \left(\frac{T_i}{T}\right)^{g_{1,i,s}} + x_a g_{0,i,a} p \left(\frac{T_i}{T}\right)^{g_{1,i,a}} \quad (20)$$

$$\Delta\nu_{0,i} = \delta\nu_{0,i,a} p \quad (21)$$

where  $w$  is the Faddeeva function (the convolution of the Doppler line profile and the Lorentz line profile [107]),  $c$  is the speed of light,  $m_i$  is the molar mass of the molecule in question,  $R$  is the universal gas constant,  $g_{0,i,s}$  is the HITRAN self broadening coefficient,  $g_{1,i,s}$  is the HITRAN self broadening temperature exponent,  $g_{0,i,a}$  is the HITRAN air/bath broadening coefficient,  $g_{1,i,a}$  is the HITRAN air/bath broadening temperature exponent, and  $\delta\nu_{0,i,a}$  is the HITRAN air/bath pressure shift.

By default, HITRAN does not provide the more complete Hartmann-Tran profile parameters [108]. ARTS can compute the Hartmann-Tran profile so it would be excellent if more data of the type were made available by default.

One additional complication not covered by any of the expressions above occurs when the atmosphere is considered in non-local thermodynamic equilibrium as this will contribute to the  $\vec{J}_n$  term of our radiative transfer calculations. Yamada et al. [109] describes the basics of the implementation in ARTS to compute non-local thermodynamic equilibrium.

### 3.2. Other absorption

Besides spectral line by spectral line absorption calculations, ARTS also includes state of the art absorption continua, such as CKD\_MT up to Version 4 for water vapor (from Version 4 on CKD\_MT water vapor continuum coefficients are stored as external data and distributed via the HITRAN website, so any later version will also work). Furthermore, HITRAN collision-induced absorption ([110], last HITRAN data access July 2022) and absorption cross section data [19] are also available, for example for halocarbons as described in [20]. Continua and other absorption functions will continue to be updated as new data become available.

## 285 4. Scattering

286 This section deals with simulations where scattering by particles within  
287 the atmosphere is considered. Particles here refers to hydrometeors (liquid  
288 or frozen cloud and precipitation particles) or aerosols. ARTS 2.6 handles for  
289 the first time also molecular scattering (for UV/visible radiation) but this is  
290 described in another article. This section starts by outlining the input data  
291 required, and ends with an overview of available scattering solvers.

### 292 4.1. Particle properties

293 The combination of shapes and sizes of aerosols and hydrometeors is  
294 basically unlimited and, as a consequence, the core manner in ARTS to  
295 describe particle properties is generic by design. It is up to the user to decide  
296 what set of scattering elements to include in the calculations. The definition  
297 of a scattering element has two parts, the single scattering properties of the  
298 element and the associated number density.

#### 299 4.1.1. Single scattering data

300 ARTS has its own format for single scattering data. These data represent  
301 the extinction, absorption and scattering function, gridded as a function of  
302 frequency and temperature, of the scattering element. For a limited set of  
303 shapes, including spheroids and cylinders, the single scattering data can be  
304 calculated with a relatively low calculation burden by the T-matrix method.  
305 ARTS contains an interface to such code, the one by [111]. For more complex  
306 shapes, the scattering data have to be calculated externally. For hydrome-  
307 teors and calculations at frequencies between 1 and 900 GHz, the ARTS  
308 infrastructure contains an extensive database of precomputed values. This  
309 ARTS single scattering database consists of two parts. The broadest selection  
310 of habits (i.e., shape model) is offered for the standard assumption of totally  
311 random orientation (TRO), for details see [17]. The ARTS format can also  
312 represent particles that just have azimuthally random orientation (ARO).  
313 The corresponding part of the database contains data for two habits [18].  
314 Data from other databases covering cloud ice particles have been converted  
315 to the ARTS format and been applied. We are not aware of any application  
316 of ARTS involving scattering by aerosols, but this should in principle also be  
317 possible.

#### 4.1.2. Particle number densities and size distributions

The user can opt to directly import particle number densities for the chosen scattering elements, if such are at hand from an external source or are calculated on the Python side. However, more common is the case that the user has bulk properties, such as condensate mass concentrations, and from this wants to generate particle number concentrations that follow a particle size distribution (PSD). To simplify this process, a number of PSD parameterisations are included in ARTS. For clarity, it should be noted that a PSD is a continuous size distribution (for example in units of  $\#/(m^3 \cdot m)$ ), while derived particle number densities are values integrated/binning in size (for example in units of  $\#/m^3$ ).

First of all, there is a set of methods for treating the PSD as a modified gamma distribution (MGD), implemented following the nomenclature and equations of [112]:

$$n(x) = N_0 x^\mu e^{-\Lambda x^\gamma}, \quad (22)$$

where the four MGD parameters are  $N_0$ ,  $\mu$ ,  $\Lambda$ , and  $\gamma$ , and  $x$  is the measure on size. To allow analytical expressions for all needed operations, the relationship between size and mass must follow a power-law:

$$m = ax^b. \quad (23)$$

As long as Eq. 23 can be fulfilled,  $x$  can represent any selection of size. For example, to let  $x$  represent mass, both  $a$  and  $b$  have to be set to 1. See [112] for further choices.

The MGD methods allow that  $N_0$ ,  $\mu$ ,  $\Lambda$  and  $\gamma$  all vary throughout the atmosphere, but can also be set to be constant. That is, the user can operate with up to four moments. There are methods for expressing one moment as bulk mass  $[kg/m^3]$ , possibly combined with a second bulk property. This second moment can be: number density, mean particle mass, mean size and median size. There is also a MGD method handling the common assumption of a power-law relationship between  $N_0$  and  $\Lambda$ . The generic PSD methods include also two methods for setting up mono-dispersive distributions.

There are several PSD methods specific for hydrometeors. For rain the PSDs of [113] and [114] are included. The classical rain PSD of [115] is covered by the general MGD methods. For ice hydrometeors, the parameterisations of [116], [117], [118] and [119] are included. Also included are two PSD schemes matching multimoment microphysics schemes common in atmospheric models [120, 121].

346 All these methods can provide the derivative of the PSD with respect  
347 to free parameters (that is, the moments used). This is a prerequisite to  
348 perform OEM inversions of observations involving scattering. However, just  
349 two of the scattering solvers can actually make use of this feature, see below.

#### 350 4.2. Scattering solvers

351 Algorithms performing radiative transfer in the presence of scattering  
352 are referred to as scattering solvers. Common to these algorithms is that  
353 they solve the problem that, due to scattering, radiation traveling in a given  
354 direction depends on the radiation in all other directions at the same point.  
355 Expressed in the mathematics of section 2.1, the computation of the  $\vec{J}_s$  term  
356 in Equation 14 would require an integral over the radiation Stokes vector  
357  $\vec{I}$  from all incoming directions, weighted by the scattering phase matrix,  
358 making the simple solution of integrating along a single line of sight, as in  
359 Equation 3, impossible.

360 Different scattering solvers employ different strategies to overcome this.  
361 In doing so, they use their own internal representation of the radiation field,  
362 and their own intrinsic approximations and simplifications, such as scalar  
363 (unpolarized) radiation only, one-dimensional atmospheres, and often plane-  
364 parallel geometry. It goes beyond the scope of this text to discuss the different  
365 solver strategies, good overviews are given for example in [122, 123, 124, 125].  
366 Instead, the goal here is to describe the solvers that are available in ARTS,  
367 along with their strengths and limitations, where limitations include those  
368 that are intrinsic to the solver and those related to our implementation or  
369 the coupling to ARTS.

370 ARTS comes with two types of scattering solvers, a set for calculating  
371 scattering of thermal emission, resulting in radiances, and two methods for  
372 simulating radar reflectivity measurements. These are described in separate  
373 subsections below.

##### 374 4.2.1. Radiances

375 The discrete ordinate iterative (DOIT) [2] and the Monte Carlo (MC)  
376 [6] solvers were developed directly for ARTS and were introduced by [12].  
377 More recently, interfaces to two external scattering solvers have been added,  
378 namely DISORT and RT4. The MC module is restricted to simulate re-  
379 mote sensing observations, while DISORT, DOIT and RT4 provide the full  
380 radiance field and can thus also form the basis for flux calculations (Sec. 5).

Name	Vector	3D	PP	Flux	Comment
DISORT	No	No	Yes	Yes	Only Lambertian surface
DOIT	Yes	Yes	No	Yes	3D not recommended
Hybrid	No	Yes	No	No	Can be used with OEM
MC	Yes	Yes	No	No	Choice for detailed 3D
RT4	Yes	No	Yes	Yes	No multi-threading

Table 1: ARTS radiance scattering solvers. The columns are, starting from left: short name of the solver, if vector (polarized) radiative transfer can be made, if 3D geometry covered, if plane parallel, if suitable for flux calculations, and notable limitation or feature. Solvers having Yes below Vector can also handle particle orientation (ARO). Comments refer to the implementation in ARTS, and should not be taken as generally true in the case of third party solvers.

381 Table 1 gives a summary of the scattering solvers covered by this section and  
382 their individual limitations.

383 The DISORT approach [126] is arguably the most established scattering  
384 solver in our field and exists in several implementations. ARTS is coupled to  
385 the code of [103]. In contrast to other scattering solvers in ARTS, DISORT is  
386 limited to unpolarized (scalar) calculations and thus also to totally random  
387 particle orientation (TRO).

388 The RT4 solver [127] fits better with the general functionality of ARTS. It  
389 handles polarized radiation and scattering data for both TRO and ARO and  
390 it can be coupled to ARTS own description of specularly reflecting surfaces.  
391 A limitation of RT4 compared to DISORT is that scaling with respect to  
392 the forward scattering peak is missing. RT4 also can not yet be used with  
393 multi-threading inside ARTS, mainly as RT4 comes as FORTRAN code.

394 Both DISORT and RT4 assume a plane-parallel atmosphere (in other  
395 words an infinite planet radius), while remaining parts of ARTS operate with  
396 a spheroidal reference geoid. Another deviation to ARTS is that RT4 and  
397 DISORT take layer-means as input, while ARTS operates with point values  
398 (assuming a linear variation, in each spatial dimension, between grid points).  
399 To overcome this difference, an averaging is performed between the altitude  
400 levels of ARTS. That is, if the ARTS pressure grid has  $n$  points, DISORT  
401 and RT4 will be used with  $n-1$  layers. This difference in discretization can be  
402 significant if comparing radiances between scattering solvers inside ARTS.

403 To extend the usage of the scattering solvers of 1D character, an inde-  
404 pendent beam approximation (IBA) wrapper method has been implemented.  
405 This method allows to apply the 1D solvers in simulations of remote sensing



406 data done using 2D and 3D atmospheres. The IBA strategy is to calculate  
407 the propagation path through the 2D or 3D atmosphere, and interpolate the  
408 atmospheric and surface fields to the points of the path. After the inter-  
409 polation, the obtained values are used to create a, likely slanted, 1D view  
410 of the atmosphere. The final radiances for the simulation are obtained by  
411 interpolating, in angles, the radiation field given by the scattering solver  
412 based on the obtained 1D view. By applying IBA repeatedly it is possible  
413 to incorporate inhomogenities inside the footprint of microwave sensors with  
414 relatively small errors compared to full 3D MC calculations [72]. For obser-  
415 vations resulting in that the propagation path does not cover all altitudes  
416 (such as airborne upward observations), the atmosphere is sampled vertically  
417 to cover the missing altitude range, starting from the observation point.

418 None of the scattering solvers mentioned above provides the Jacobian,  
419 which is a prerequisite for OEM-type retrievals (see Sec. 6). As a first step  
420 to overcome this limitation, a hybrid method has been implemented. In  
421 short, either DISORT, DOIT or RT4 is first run to obtain the full radiance  
422 field. The hybrid method performs an integration following Eq. 3, where the  
423 pre-calculated radiance field is used to calculate the scattering source term  
424 ( $\vec{J}_s$  in Eq. 14). The general approach for deriving the Jacobian in ARTS has  
425 been extended to cover this case, but with the limitation that the incoming  
426 radiation field is assumed constant. That is, the provided Jacobian ignores  
427 the fact that a change at one point in the atmosphere can affect the scattering  
428 source term at another point. Thus the Jacobian is not fully exact, but tests  
429 showed that retrieval convergence can be achieved in most cases and the  
430 method has been applied successfully in remote sensing applications [68, 69].

431 We will end this subsection with a usage example: Fox et al. [128] used  
432 ARTS to evaluate the representation of ice clouds in a Numerical Weather  
433 Prediction (NWP) model. The Monte Carlo scattering solver was used to  
434 simulate passive sub-millimeter wave brightness temperatures from 3D NWP  
435 model input fields using ice crystal scattering properties from the ARTS  
436 database [17], and these were compared to airborne observations. Figure 1  
437 shows an example of the simulated and observed brightness temperatures  
438 between 157 and 874 GHz, and the NWP model hydrometeor fields used  
439 as input to the simulations. This example used the scattering properties  
440 of the large column aggregate particle type from the scattering database to  
441 represent the cloud ice. The study demonstrated that ARTS is capable of  
442 simulating realistic brightness temperatures across the full range of frequen-  
443 cies used, when appropriate ice crystal scattering models are selected.

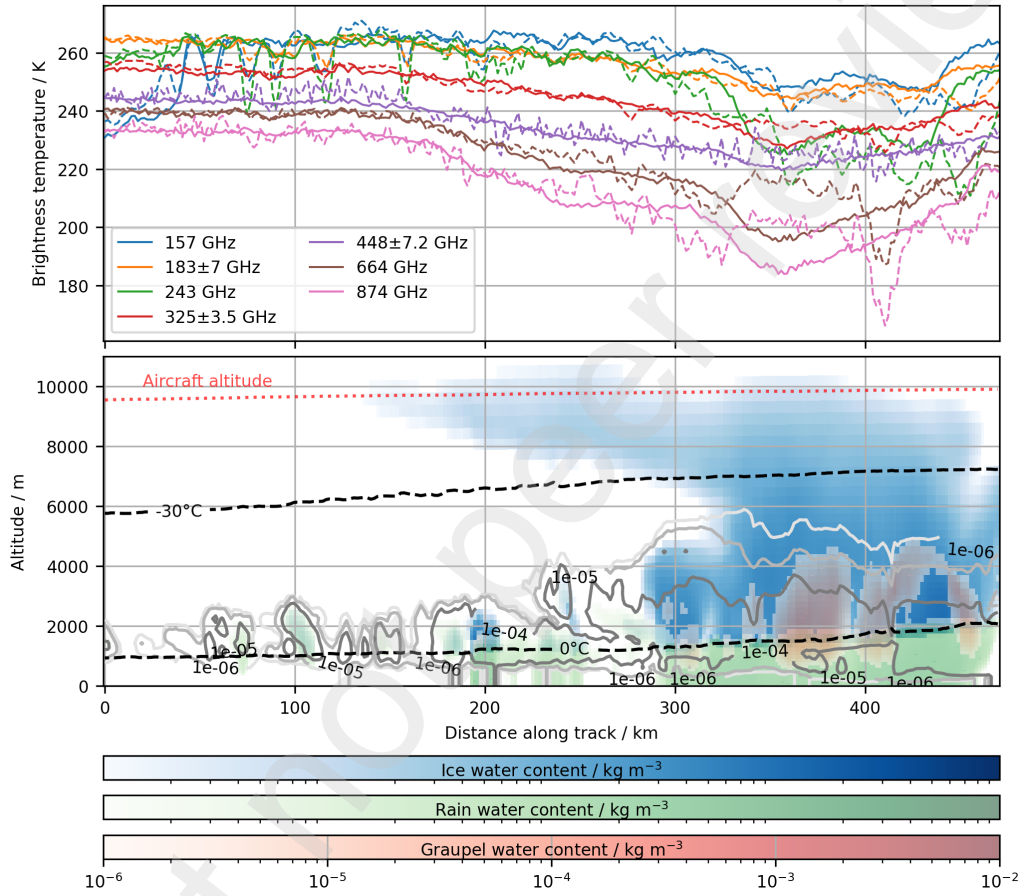


Figure 1: Top panel: Simulated (solid lines) and observed (dashed lines) brightness temperatures between 157 and 874 GHz from a passive airborne radiometer viewing a cloudy scene. Bottom: Cross-section of the cloud fields from the NWP model used as input to the simulations. The colours represent the ice, rain and graupel water contents, and the gray contours represent the cloud liquid water content.

#### 4.2.2. Radar measurements

ARTS contains two methods for simulating atmospheric monostatic radar observations. Their complexity depends strongly on whether multiple scattering is significant or not. As a consequence, there are two distinct radar methods.

For **single scattering** only simulations, the calculation is very straightforward, and the core task is to determine the bulk backscattering and weigh it with the two-way transmission:

$$\mathbf{s}_b = \mathbf{T}\mathbf{Z}_b\mathbf{T}\mathbf{s}_t, \quad (24)$$

where  $\mathbf{s}_t$  is the unit Stokes vector describing the polarisation state of the transmitted radar pulse,  $\mathbf{Z}_b$  is the bulk scattering matrix for the point of concern in the back-scattering direction,  $\mathbf{T}$  is the Mueller transmission matrix for the distance between the radar transmitter/receiver and the backscattering point, and  $\mathbf{s}_b$  is the Stokes vector for the returned pulse.

The transmission matrix for the away and home directions can theoretically differ (for vector calculations, not for scalar ones), but this should be of no practical concern and is ignored here. Furthermore, the method allows to scale the extinction going into  $\mathbf{T}$ . This is a scalar value,  $r_e$ , with one as default. By setting  $r_e = 0$ , the unattenuated return pulse is obtained. At least for some situations, a full calculation with multiple scattering ends up roughly halfway between  $r_e = 0$  and  $r_e = 1$  [129], and setting  $r_e \approx 0.5$  could be considered for approximating the neglect of multiple scattering.

This single-scattering method provides the full Jacobian. That is, the Jacobian includes derivatives with respect to both  $\mathbf{Z}_b$  and  $\mathbf{T}$ . OEM retrievals using this method are found in papers by Pfreundschuh et al. [68, 69].

For **multiple scattering** simulations, the calculation becomes more complex. For simulating atmospheric profiling pulse radar, the calculation of scattering events has to be considered within the context of pulse propagation time. Additionally, to avoid overestimating multiple scattering effects and properly account for the relationship between beam size and multiple scattering, simulations require a finite antenna pattern [130, 131].

Following studies by Marzano et al. and Battaglia et al. [132, 131], ARTS uses a Monte Carlo approach to account for multiple scattering effects from hydrometeors in the atmosphere. All scattering events have the potential to contribute to the simulated backscatter profile, so backward ray tracing would not produce any computational advantage unlike those realized for

476 passive sensing [for example 6]. Therefore, ray tracing initiates from the  
477 transmitter using traditional forward Monte Carlo sampling.

478 Each discrete contribution to the radiative transfer solution is initiated  
479 by drawing two random numbers from a bivariate Normal distribution with  
480 means aligned with the sensor boresight and standard deviations related to  
481 the antenna full-width, half-maximums (FWHM) of the E- and H-planes of  
482 the antenna pattern, where  $\sigma = FWHM/2.3548$ . This procedure determines  
483 the direction of the line-of-sight for the radiative transfer contribution under  
484 the assumption of a Gaussian antenna pattern.

485 Next to calculate propagation path length, a random number  $r_p$  drawn  
486 from a uniform distribution represents the scalar path transmission corre-  
487 sponding to the extinction of the first Stokes element  $I$ . Starting with a  
488 scalar transmission coefficient  $t_I = 1$ , the path transmission matrix is ac-  
489 cumulated while  $t_I > r_p$ . For cases in which the bulk extinction matrix  
490 is block-diagonal due to contributions from azimuthally-random particles,  
491 transmission includes the effects on cross-polarization based on the state of  
492 the Stokes vector at the beginning of the propagation path. When  $t_I \leq r_p$ ,  
493 propagation ends and the accumulated transmission matrix, and correspond-  
494 ing path length, are stored.

495 After path length and transmission calculation, the bulk scattering prop-  
496 erties are calculated at the propagation path end. Random number  $r_a$  is  
497 drawn from a uniform distribution and compared with albedo  $\alpha$ , or the ratio  
498 of scattering cross-section  $C_{sca}$  over extinction cross-section  $C_{ext}$ . If  $\alpha < r_a$ ,  
499 propagation is terminated at an extinction event; otherwise, the monostatic  
500 backscatter contribution is recorded for the radar range bin corresponding to  
501 the calculated path length. This contribution includes the normalized trans-  
502 mission in the transmit direction, to account for polarization mixing, return  
503 transmission, and weighting for the receiver Gaussian antenna pattern.

After accounting for the scattering event, the process restarts, this time  
with uniform random variables  $r_{ze}$  and  $r_{az}$  providing the zenith and azimuth  
scattering directions, and a new starting (scattered) stokes vector  $\mathbf{I}_s$  is calcu-  
lated from the product of the phase matrix  $\mathbf{Z}$  and the incident Stokes vector  
 $\mathbf{I}_i$ :

$$\mathbf{I}_s = \mathbf{Z}(\theta_i, \theta_s, \Delta\phi)\mathbf{I}_i \quad (25)$$

504 where  $\theta$  is the zenith angle and  $\Delta\phi$  is the difference of the scattered and inci-  
505 dent azimuth angles. Subscripts  $i$  and  $s$  correspond to incident and scattered,  
506 respectively.

507 At subsequent scattering events, bistatic scattering for the incident and  
508 scattered angles contributes to the accumulated backscattering at the range  
509 bin corresponding to the total distance traveled before the scattering event.  
510 Path tracing ends, at an absorption event, when  $I$  falls below a predetermined  
511 threshold, or when the maximum specified scattering order is reached. A  
512 scattering order of 1 is equivalent to single scattering. For multiple scattering  
513 simulations, the suggested scattering order is 20 based on use across a range  
514 of cloud types.

515 Figure 2 shows an example simulation, a hypothetical space-based nadir-  
516 pointing W-band radar, comparing single scattering (top panel) and multiple  
517 scattering (middle panel) simulations, with differences shown at the bottom.  
518 The top simulation uses the ARTS single scattering solver convolved with a  
519 Gaussian antenna pattern such that the field of view at the surface is 1 km.  
520 As expected, the largest multiple scattering enhancement corresponds to the  
521 convective cells and the surrounding regions. Multiple scattering results in  
522 excess reflectivity where the W-band signal is otherwise being extinguished,  
523 but this large enhancement is decorrelated from the vertical structure of the  
524 cloud along the radar line of sight. There are two features to note. The  
525 multiple scattering simulations are noisy at cloud edges and miss some thin  
526 clouds captured in the single scattering simulation. This is due to the large  
527 number of ray traces, on the order of  $5e5$ , needed to resolve the simulations.  
528 While runtime is linear with the number of ray traces, the ray tracing routine  
529 is not trivial in terms of runtime. Thus, this simulator should be used only  
530 when multiple scattering is suspected.

## 531 5. Radiative energy flux and heating rate calculations

### 532 5.1. Fluxes

533 ARTS is suitable for accurate reference calculations of atmospheric ener-  
534 getics: radiative energy fluxes and associated heating rates. As an example,  
535 Roemer et al. [133] used it to investigate the longwave radiative feedback  
536 from a spectrally resolved perspective. To this end, spectral irradiance ( $\mathcal{L}_\nu$ )  
537 at the top of the atmosphere was calculated for a set of idealised atmo-  
538 spheres, using the existing interface between ARTS and the single-column  
539 radiative-convective equilibrium model konrad [89, 134]. Figure 3 shows some  
540 of those  $\mathcal{L}_\nu$  spectra between  $10\text{ cm}^{-1}$  and  $2,500\text{ cm}^{-1}$  for surface temperatures  
541 of 268 K, 288 K, and 308 K, representing the spatial variations of Earth's sur-

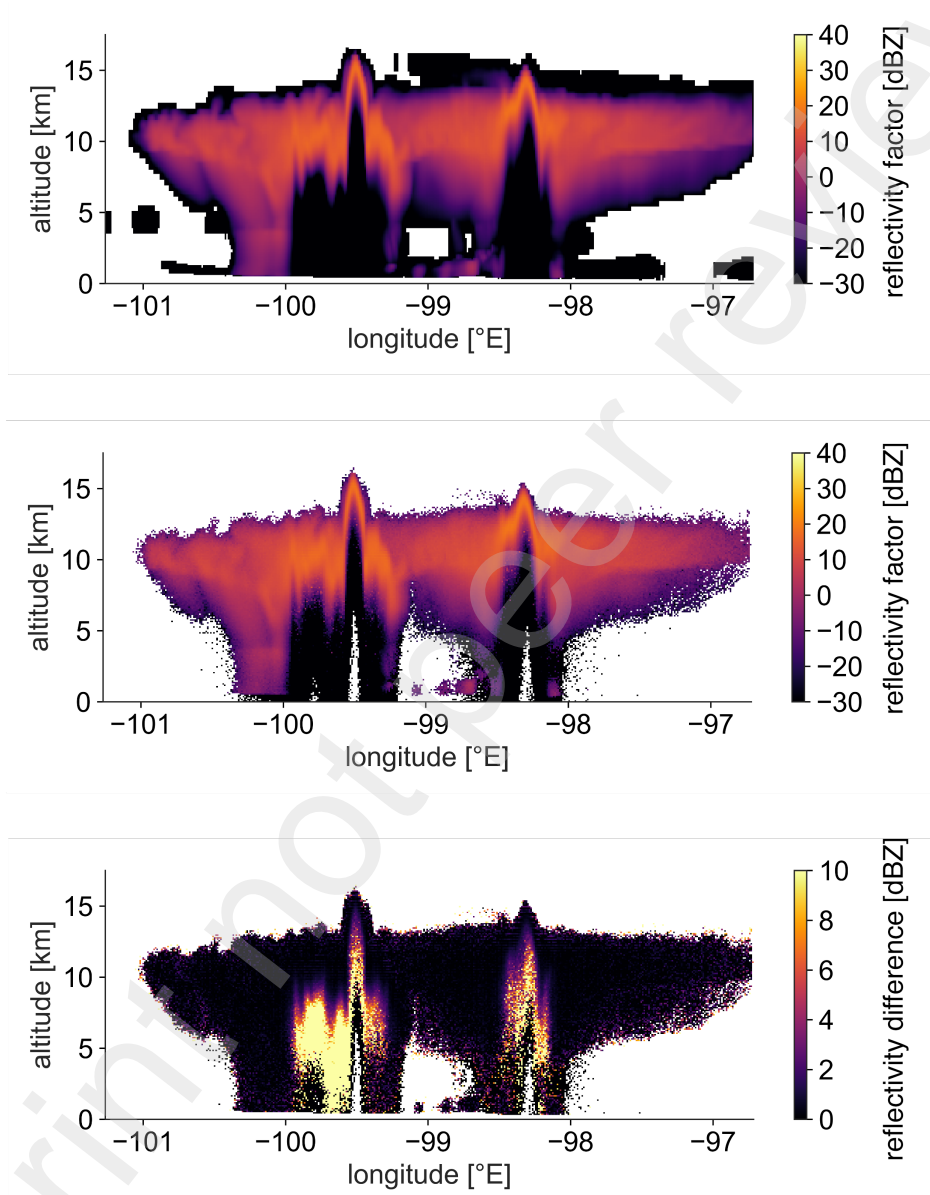


Figure 2: Top panel: W-band single scattering simulation of convective cells and associated anvil. Middle panel: Multiple scattering simulation of same cloud field as top. Bottom panel: Difference of middle and top showing the enhancement due to multiple scattering.

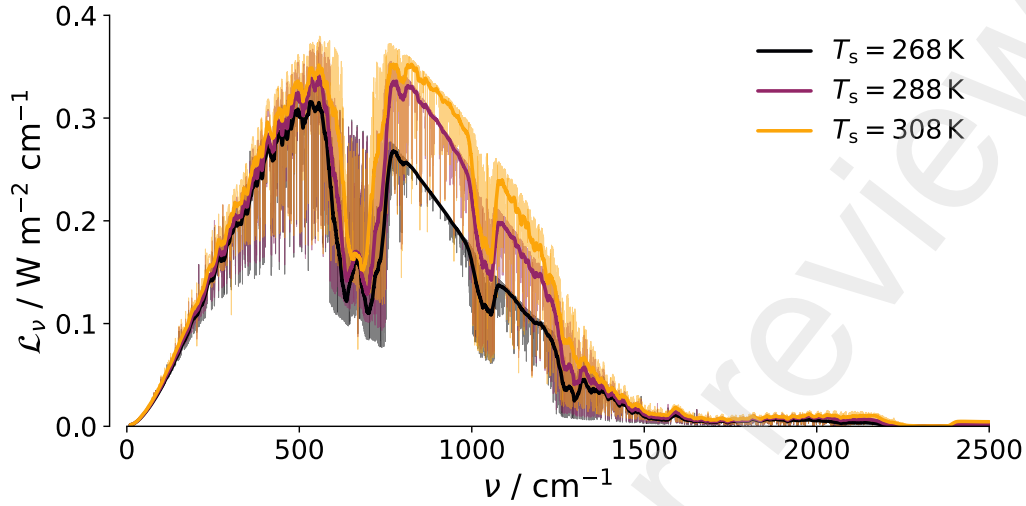


Figure 3: Simulated spectrally resolved outgoing longwave radiation  $\mathcal{L}_\nu$  as a function of wavenumber  $\nu$  for idealised atmospheres with different surface temperatures  $T_s$ . Shown are the spectra at a spectral resolution of  $0.1 \text{ cm}^{-1}$  (thin lines, perhaps invisible in printed version) and the  $20 \text{ cm}^{-1}$  moving averages (thick lines).

face temperature. Those simulations were then used to better understand the spectral longwave feedback derived from satellite observations.

Another very recent usage example of this capability is the study by He [135] that used ARTS for reference calculations of instantaneous  $4\times\text{CO}_2$  forcing at different surface temperatures.

Spectral irradiance is calculated by integrating spectral radiance, the native quantity of ARTS radiative transfer (the first component of the Stokes vector introduced in Equation 1) over one hemisphere. More correctly speaking, it is the component normal to a horizontal surface that is integrated. Integrating spectral irradiance over frequency then gives the total irradiance, that is, the total radiative energy flux in units of  $\text{W}/\text{m}^2$ . We define fluxes as a directed quantity in the context of 1D atmospheres, positive fluxes are directed upwards, negative fluxes are directed downwards, and the net flux is defined as the sum of the upward and downward flux.

ARTS has several ways to calculate radiation fluxes. For clear-sky fluxes there is an internal method, which uses the internal clear-sky radiative transfer solver to calculate spectral radiances. It assumes a plane parallel atmosphere, for consistency with the all-sky solvers described below.

560 For all-sky fluxes, one can in principle use any of the discrete ordinate  
561 solvers available in ARTS, that is DISORT, RT4 and DOIT to calculate  
562 spectral radiances and then integrate them as mentioned above using in-  
563 ternal integration methods. Due to the higher complexity when handling  
564 scattering, all-sky flux simulations are in general several times slower than  
565 clear-sky flux simulations. To mitigate this, we recommend to use DISORT  
566 as it is much faster than RT4 and DOIT and advanced features of the other  
567 solvers like polarization are of less interest for flux calculations. Furthermore,  
568 ARTS supports a dedicated DISORT mode for simulating fluxes, in which  
569 the integration over the hemisphere is done internally and very efficiently.

570 The flux simulation can be done with an arbitrary number of zenith an-  
571 gles over which the angular integration is done, and an arbitrary number of  
572 frequencies over which the spectral integration is done. As a rule of thumb,  
573 to get an accuracy in the order of  $1 \text{ W m}^{-2}$  for the fluxes, the number of  
574 zenith angles should be at least 6 and the number of frequencies should be  
575 in the order of several thousand. For reference calculations the number of  
576 frequencies should be even in the order of several ten thousand.

577 The left-hand column of Figure 4 illustrates ARTS' capability of simulat-  
578 ing long wave and short wave net fluxes for a modeled tropical atmosphere  
579 over the eastern Pacific with a thin liquid water cloud on top of the boundary  
580 layer. Reference flux calculations for all-sky and clear-sky were done using  
581 ARTS-DISORT with 30,000 frequencies and 10 streams.

582 An interesting option for efficient flux calculations is that ARTS ships  
583 with a set of representative frequencies and associated quadrature weights  
584 derived by Paulina Czarnecki [136]. Stated very briefly, the idea is that a  
585 weighted mean over the spectral flux at these few frequencies gives an ac-  
586 curate estimate of the total flux. They are identified from high spectral  
587 resolution reference calculations for a diverse set of atmospheres by a com-  
588 bination of simulated annealing and linear regression, a method that was  
589 originally developed for efficiently simulating satellite observations [10]. In  
590 this case there are 64 representative frequencies each for longwave and short-  
591 wave. The calculations with this method are  $30,000/64 \approx 470$  times faster  
592 than the reference calculations, results are marked with dots in Figure 4,  
593 illustrating the close agreement.



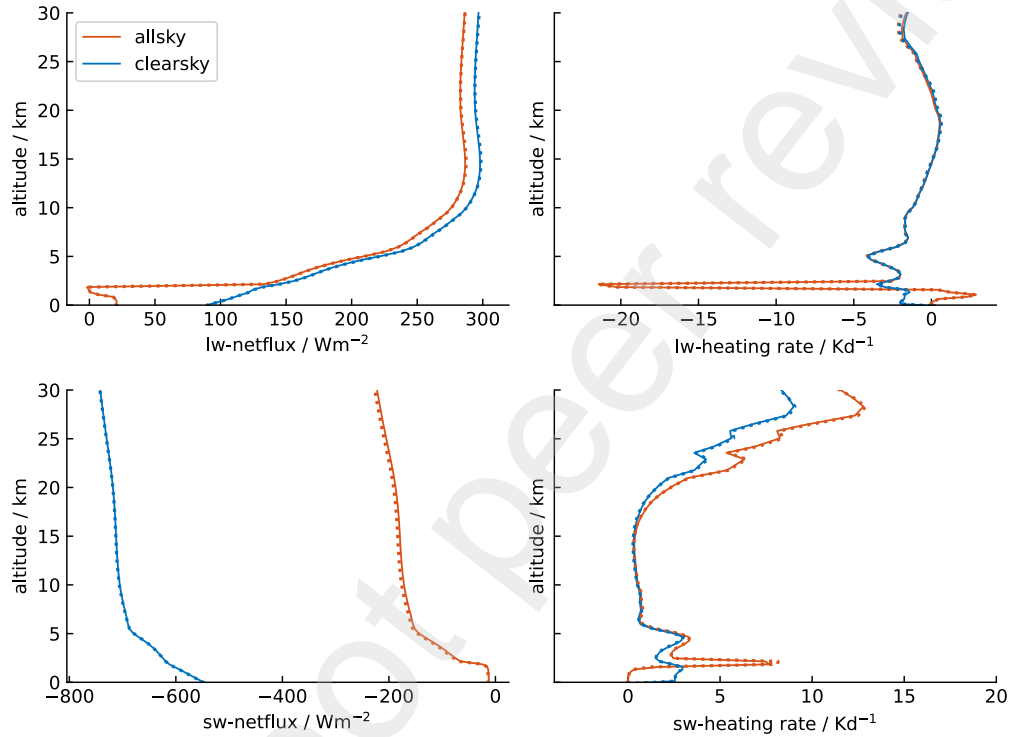


Figure 4: Simulation results for a modeled tropical atmosphere over the eastern Pacific with a thin but dense liquid water cloud on top of the boundary layer (peak liquid water content  $0.4 \text{ g/m}^3$  at  $1.3 \text{ km}$  altitude, liquid water path  $500 \text{ g/m}^2$ ). Solid lines show the reference setup and dots show the fast setup. Top left: All sky and clear sky long wave net flux. Bottom left: All sky and clear sky short wave net flux. A positive net flux denotes a net upward flux and a negative net flux a net downward flux. Top right: All sky and clear sky long wave heating rates. Bottom right: All sky and clear sky short wave heating rates.

## 594 5.2. Heating rates

Based on the fluxes, ARTS also calculates radiative heating rates. Assuming hydrostatic equilibrium, the heating rate  $H$  is defined as

$$H = \frac{g}{c_p} \frac{dF_{net}}{dp}, \quad (26)$$

595 where  $g$  is the gravitational acceleration,  $c_p$  is the mass specific heat capacity  
 596 at constant pressure and  $F_{net}$  is the net flux. The derivative is internally  
 597 approximated with a central difference and for the edges with a polynomial  
 598 interpolation, which both are second order accurate. With this approxima-  
 599 tion, the heating rates are calculated on the same grid as the atmospheric  
 600 state. The specific heat capacity  $c_p$  depends on temperature and pressure  
 601 and has to be provided by the user. The gravitational acceleration  $g$  de-  
 602 pends on altitude, latitude and longitude and is calculated internally. In the  
 603 following example,  $c_p$  is set constant to the mass specific heat capacity of dry  
 604 air  $c_{p,air} = 1005.7 \text{ J kg}^{-1} \text{ K}^{-1}$  and  $g$  is varying with altitude.

605 The right column of Figure 4 shows the all-sky and clear-sky long wave  
 606 (top) and short wave (bottom) heating rates for the selected example case.  
 607 The liquid cloud causes strong cooling at the cloud top and weaker but also  
 608 significant heating at the cloud bottom. Dots again mark the fast approx-  
 609 imation using the representative frequencies and weights. The very good  
 610 agreement shows that the fast scheme is a very attractive option when spec-  
 611 tral information is not needed.

612 Note that the reason why the fast scheme works so well for heating rates  
 613 is that heating rates were included as a training target, in addition to fluxes,  
 614 in the derivation of the frequencies and weights [136]. This is necessary,  
 615 because small fluctuations in the flux can have a large impact on its altitude  
 616 gradient, the heating rate. This is particularly true at higher altitudes where  
 617 the heat capacity is small due to low pressure.

618 Note also, though, that the training for the representative frequencies  
 619 and weights was completely based on clear-sky simulations. It is therefore  
 620 not completely self-understood that they would work equally well for all-sky  
 621 simulations, as the figure seems to indicate, although we had hypothesized  
 622 that this would be the case. The argument in favor of this is that clouds tend  
 623 to make the radiation field more homogeneous across different frequencies,  
 624 which makes the exact positions of the quadrature frequencies less critical.  
 625 We have not yet done a proper quantitative evaluation of the accuracy of the  
 626 fast scheme for all-sky simulations, but these first results seem promising.

627 Finally, it is worth mentioning that the representative frequencies and  
628 weights so far were only trained for present-day variations of water vapor,  
629 ozone, temperature and different CO<sub>2</sub> levels. There is work in progress on  
630 expanding that to variability in all greenhouse gases but for now the scheme  
631 will probably not work well for large perturbations in parameters not covered  
632 in the above list, for example for a significantly different methane concentra-  
633 tion.

## 634 6. Optimal estimation retrievals

635 ARTS has supported retrievals since its first version by providing the  
636 Jacobian, but there has not been any built-in retrieval method. The standard  
637 alternative has been Qpack [4], providing a Matlab implementation of the  
638 optimal estimation method (OEM, [137]). OEM has now been integrated  
639 into ARTS, and, compared to [4], more efficient calculations and options can  
640 be offered.

### 641 6.1. Overview

642 The OEM is based on a Bayesian formulation of the inverse problem of  
643 finding an atmospheric state  $\vec{x}$  consistent with a vector  $\vec{y}$  of remote sensing  
644 observations using a forward model  $F : \vec{x} \rightarrow \vec{y}_f$  that allows simulating ob-  
645 servations corresponding to a given atmospheric state  $\vec{x}$ . The OEM is based  
646 on the assumptions that (1) the error affecting the observations is bias-free  
647 Gaussian noise with covariance matrix  $\mathbf{S}_e$  and that (2) a priori knowledge of  
648 the atmospheric state  $\vec{x}$  can be described using a Gaussian distribution with  
649 a priori state  $\vec{x}_a$  and a priori covariance matrix  $\mathbf{S}_a$ . By application of Bayes'  
650 theorem, the posterior distribution, which fully describes the solution of the  
651 inverse problem, is found to be (up to a normalization constant):

$$p(\vec{x}|\vec{y}) \propto \exp \left( -\frac{1}{2}(F(\vec{x}) - \vec{y})^T \mathbf{S}_e^{-1} (F(\vec{x}) - \vec{y}) - \frac{1}{2}(\vec{x} - \vec{x}_a)^T \mathbf{S}_x^{-1} (\vec{x} - \vec{x}_a) \right) \quad (27)$$

If the underlying assumptions of the OEM hold true, the posterior distribution is Gaussian, too, and is fully specified by its mean and covariance matrix. The mean of the posterior distribution, which, due to the Gaussian nature of the posterior distribution, coincides with the maximum-a-posteriori

estimator of  $\vec{x}$ , is typically found by minimizing the negative log-likelihood of (27), which is given by

$$-\log(p(\vec{x}|\vec{y})) = \frac{1}{2}(F(\vec{x}) - \vec{y})^T \mathbf{S}_e^{-1}(F(\vec{x}) - \vec{y}) + \frac{1}{2}(\vec{x} - \vec{x}_a)^T \mathbf{S}_x^{-1}(\vec{x} - \vec{x}_a) \quad (28)$$

652 Finding the posterior mean state of the inverse problem thus boils down  
653 to minimizing Equation 28. If the forward model  $F$  is linear, a global mini-  
654 mum of Equation 28 can be found in a single step using the Gauss-Newton  
655 method. However, for most applications in atmospheric remote sensing the  
656 forward model  $F$  is non-linear. In this case, Equation (28) has to be mini-  
657 mized iteratively. In addition to the Gauss-Newton (GN) method, the ARTS  
658 OEM method also provides an implementation of the Levenberg-Marquardt  
659 method (LM), which tends to be more stable for strongly non-linear forward  
660 models, such as those involving scattering.

661 Apart from the evaluation of the forward operator  $F$ , the computationally  
662 most complex operation in the application of the GN and LM optimizers  
663 is the solving of a linear system of equation, having a size following the  
664 number of elements in  $\vec{x}$ . Since solving such a linear system of equations  
665 explicitly may become prohibitively expensive in terms of computation time  
666 and memory, all optimization methods in ARTS can be used with a conjugate  
667 gradient (CG) solver. The CG method solves the linear system iteratively  
668 and becomes computationally more efficient as the number of variables in  $\vec{x}$   
669 grows large.

## 670 6.2. ARTS integration

671 The ARTS OEM method aims to retain most of ARTS' flexibility in terms  
672 of performing forward simulations. To provide a maximum of flexibility in  
673 terms of forward model calculations, the OEM module interfaces with the rest  
674 of ARTS by an agenda. This agenda typically performs the following steps:

- 675 1. Unpack the vector  $\vec{x}$  into the corresponding atmospheric fields and  
676 convert the elements to the forward model units,
- 677 2. perform the forward simulation,
- 678 3. apply required variable transformations to the Jacobian

679 Due to the flexibility of ARTS agendas this design allows most of ARTS'  
680 functionality to be used in a retrieval.

681 A principal benefit of the OEM integration into ARTS is that ARTS pro-  
682 vides built-in functions that map elements of  $\vec{x}$  to atmospheric fields and

683 back. Moreover, retrieval grids may deviate from the forward model grids.  
684 Although the retrieval grid is not allowed to be broader than the correspond-  
685 ing forward model grid, it can cover a smaller range. Retrieved values are  
686 mapped to the forward model grids by using linear interpolation inside the  
687 ranges of the retrieval grids, and using nearest neighbour outside. That is,  
688 values at end points of retrieval grids are assumed to be valid all the way  
689 to end points of the forward model grids. ARTS also provides functional-  
690 ity to retrieve transformed variables and apply clipping, which helps avoid  
691 unphysical states that may lead to errors in the forward model calculation.

### 692 *6.3. Handling of a priori and error covariance matrices*

693 The calculations required to perform an OEM minimization step involve  
694 only the inverses of the covariance matrices  $\mathbf{S}_x$  and  $\mathbf{S}_e$ . Since, depending on  
695 the retrieval problem at hand, the covariance matrices can grow relatively  
696 large, ARTS allows them to be provided either as  $\mathbf{S}_x$  and  $\mathbf{S}_e$  or directly as  
697 their inverses  $\mathbf{S}_x^{-1}$  and  $\mathbf{S}_e^{-1}$ , respectively. In conjunction with the CG solver,  
698 this can drastically reduce memory requirements of the OEM calculation  
699 step and thus allow for the retrieval of a larger number of variables and  
700 observations simultaneously.

701 ARTS covariance matrices are represented as block-diagonal matrices,  
702 where each block can be provided either as normal covariance matrix or its  
703 inverse. Moreover, covariance matrix blocks can be dense or sparse matrices.  
704 This design supports the basic use case in which the user simply provides the  
705 covariance matrices but also allows for optimization of the memory footprint  
706 of the inversion by providing pre-computed and potentially sparse covariance  
707 matrices. The full covariance matrix can be represented as a single block, to  
708 allow full generalisation in the specification of correlations between variables.

## 709 **7. Summary**

710 This article gave an overview of the capabilities and limitations of ARTS  
711 version 2.6.

712 ARTS can compute atmospheric absorption by gases efficiently and ac-  
713 curately across the entire spectrum, from the radiowave to the UV/visible  
714 spectral range, including advanced features such as line mixing. Besides  
715 spectral line by spectral line absorption calculations, it also includes state  
716 of the art absorption continua, HITRAN collision-induced absorption, and a  
717 simple polynomial model fitted to HITRAN absorption cross-sections, which

718 can be used for example for halocarbon species for which spectroscopic data  
719 are typically not available [20].

720 In the longwave spectral range, ARTS is established and well tested for  
721 both clear-sky and all-sky radiative transfer simulations. In the clear-sky case  
722 (without scattering) it uses its own native radiative transfer solver, which  
723 includes analytical Jacobians. It is fully polarized and includes advanced  
724 features such as an accurate treatment of Zeeman splitting.

725 For all-sky radiative transfer simulation, ARTS offers broad support to  
726 cover microwave scattering due to hydrometeors. Inside this domain, the  
727 main consideration for the future is to improve the calculation efficiency. It is  
728 today costly to make simulations with a high number of scattering elements,  
729 and one way forward is to allow specifying bulk scattering properties directly.  
730 A full re-implementation of the handling of scattering data is ongoing to  
731 open up for this development, as well as obtaining a more uniform code base  
732 around the different scattering solvers.

733 Based on the radiative transfer simulations, ARTS can also perform en-  
734 ergy flux and heating rate calculations for both clear-sky and all-sky con-  
735 ditions. Furthermore, it has built-in methods for optimal-estimation-type  
736 retrievals of atmospheric state properties from remote observations.

737 Very recently, ARTS was extended to include a solar source term, so  
738 that it can simulate also clear-sky and all-sky shortwave radiative transfer  
739 simulations and based on that shortwave energy fluxes and heating rates.  
740 This new functionality is the subject of a separate article that is currently  
741 in preparation. Calculations with the shortwave part have so far considered  
742 molecular (Rayleigh) scattering and scattering by hydrometeors. Aerosol  
743 scattering (and absorption) could in principle be handled as well, but so far  
744 there are no ready-made databases of aerosol optical properties in the ARTS  
745 format.

746 Last but not least, it should be mentioned that ARTS is also used as  
747 a teaching tool in the international Master program Atmospheric Science at  
748 Universität Hamburg ([https://www.mi.uni-hamburg.de/studium/20-atmo-science.](https://www.mi.uni-hamburg.de/studium/20-atmo-science.html)  
749 [html](https://www.mi.uni-hamburg.de/studium/20-atmo-science.html)) for courses on radiation and climate and on remote sensing.

## 750 Obtaining ARTS

751 The ARTS homepage, providing extensive documentation, is [https://](https://radiativetransfer.org)  
752 [radiativetransfer.org](https://radiativetransfer.org). On GitHub, ARTS can be found at [https://](https://github.com/atmtools/arts/releases)  
753 [github.com/atmtools/arts/releases](https://github.com/atmtools/arts/releases) [138]. The easiest way to obtain

ARTS is through conda ('conda install -c rttools pyarts'). Pyarts is the python interface to ARTS, providing full ARTS functionality. ARTS has been extensively tested and used on macOS, Linux, and other Unix systems. It has currently not been used or tested on Windows and there is also no conda package for Windows.

## Acknowledgments

We are grateful to Aistè Schunck for cleaning up the references, and we thank the ARTS community, in particular Vasileios Barlakas, Oleksandr Bobryshev, Jakob Dörr, Robin Ekelund, Gerrit Holl, gongxunhlj (Github handle), Lukas Kluft, Teresa Mendaza, Jana Mendrok, Jon Petersen, Marc Prange, Bengt Rydberg, Mayuri Tatiya and Takayoshi Yamada for contributing to the development of ARTS. We are also grateful to those that are active on the arts-users mailing list (<https://www.radiativetransfer.org/contact>) and help us respond to user questions. For the Hamburg authors, this work is a contribution to the Centrum für Erdsystemforschung und Nachhaltigkeit (CEN). The work at Chalmers by PE and SP was supported by the Swedish National Space Agency (grants 65/18 and 166/18).

## References

- [1] T. Kuhn, A. Bauer, M. Godon, S. A. Buehler, K. Kuenzi, Water vapor continuum: Absorption measurements at 350 GHz and model calculations, *J. Quant. Spectrosc. Radiat. Transfer* 74 (5) (2002) 545–562. doi:10.1016/S0022-4073(01)00271-0.
- [2] C. Emde, S. A. Buehler, C. Davis, P. Eriksson, T. R. Sreerekha, C. Teichmann, A polarized discrete ordinate scattering model for simulations of limb and nadir longwave measurements in 1D/3D spherical atmospheres, *J. Geophys. Res.* 109 (D24) (Dec. 2004). doi:10.1029/2004JD005140.
- [3] T. R. Sreerekha, S. A. Buehler, C. Emde, A simple new radiative transfer model for simulating the effect of cirrus clouds in the microwave spectral region, *J. Quant. Spectrosc. Radiat. Transfer* 75 (2002) 611–624.

- 785 [4] P. Eriksson, C. Jiménez, S. A. Buehler, Qpack, a general tool for in-  
786 strument simulation and retrieval work, *J. Quant. Spectrosc. Radiat.*  
787 *Transfer* 91 (1) (2005) 47–64. doi:10.1016/j.jqsrt.2004.05.050.
- 788 [5] S. A. Buehler, P. Eriksson, T. Kuhn, A. von Engeln, C. Verdes, ARTS,  
789 the atmospheric radiative transfer simulator, *J. Quant. Spectrosc. Ra-*  
790 *diat. Transfer* 91 (1) (2005) 65–93. doi:10.1016/j.jqsrt.2004.05.051.
- 791 [6] C. Davis, C. Emde, R. Harwood, A 3D polarized reversed Monte Carlo  
792 radiative transfer model for mm and sub-mm passive remote sensing in  
793 cloudy atmospheres, *IEEE T. Geosci. Remote* 43 (5) (2005) 1096–1101.  
794 doi:10.1109/TGRS.2004.837505.
- 795 [7] C. Melsheimer, C. Verdes, S. A. Buehler, C. Emde, P. Eriks-  
796 son, D. G. Feist, S. Ichizawa, V. O. John, Y. Kasai, G. Kopp,  
797 N. Koulev, T. Kuhn, O. Lemke, S. Ochiai, F. Schreier, T. R. Sreerekha,  
798 M. Suzuki, C. Takahashi, S. Tsujimaru, J. Urban, Intercomparison  
799 of general purpose clear sky atmospheric radiative transfer models  
800 for the millimeter/submillimeter spectral range, *Radio Sci.* 40 (2005).  
801 doi:10.1029/2004RS003110.
- 802 [8] S. A. Buehler, A. von Engeln, E. Brocard, V. O. John, T. Kuhn,  
803 P. Eriksson, Recent developments in the line-by-line modeling of out-  
804 going longwave radiation, *J. Quant. Spectrosc. Radiat. Transfer* 98 (3)  
805 (2006) 446–457. doi:10.1016/j.jqsrt.2005.11.001.
- 806 [9] P. Eriksson, M. Ekström, C. Melsheimer, S. A. Buehler, Ef-  
807 ficient forward modelling by matrix representation of sensor re-  
808 sponses, *Int. J. Remote Sensing* 27 (9–10) (2007) 1793–1808.  
809 doi:10.1080/01431160500447254.
- 810 [10] S. A. Buehler, V. O. John, A. Kottayil, M. Milz, P. Eriksson, Efficient  
811 radiative transfer simulations for a broadband infrared radiometer —  
812 combining a weighted mean of representative frequencies approach with  
813 frequency selection by simulated annealing, *J. Quant. Spectrosc. Ra-*  
814 *diat. Transfer* 111 (4) (2010) 602–615. doi:10.1016/j.jqsrt.2009.10.018.
- 815 [11] S. A. Buehler, P. Eriksson, O. Lemke, Absorption lookup tables in the  
816 radiative transfer model ARTS, *J. Quant. Spectrosc. Radiat. Transfer*  
817 112 (10) (2011) 1559–1567. doi:10.1016/j.jqsrt.2011.03.008.



- [12] P. Eriksson, S. A. Buehler, C. P. Davis, C. Emde, O. Lemke, ARTS, the atmospheric radiative transfer simulator, version 2, *J. Quant. Spectrosc. Radiat. Transfer* 112 (10) (2011) 1551–1558. doi:10.1016/j.jqsrt.2011.03.001.
- [13] R. Larsson, S. A. Buehler, P. Eriksson, J. Mendrok, A treatment of the Zeeman effect using Stokes formalism and its implementation in the Atmospheric Radiative Transfer Simulator (ARTS), *J. Quant. Spectrosc. Radiat. Transfer* 133 (2014) 445–453. doi:10.1016/j.jqsrt.2013.09.006.
- [14] R. Larsson, A note on modelling of the oxygen spectral cross-section in the Atmospheric Radiative Transfer Simulator — Zeeman effect combined with line mixing in Earth’s atmosphere, *Int. J. Remote Sensing* 35 (15) (2014) 5845–5853. doi:10.1080/01431161.2014.945002.
- [15] R. Larsson, B. Lankhaar, P. Eriksson, Updated zeeman effect splitting coefficients for molecular oxygen in planetary applications, *J. Quant. Spectrosc. Radiat. Transfer* 224 (2019) 431–438. doi:10.1016/j.jqsrt.2018.12.004.
- [16] R. Larsson, B. Lankhaar, Zeeman effect splitting coefficients for ClO, OH and NO in some earth atmosphere applications, *J. Quant. Spectrosc. Radiat. Transfer* 250 (2020) 107050. doi:10.1016/j.jqsrt.2020.107050.
- [17] P. Eriksson, R. Ekelund, J. Mendrok, M. Brath, O. Lemke, S. A. Buehler, A general database of hydrometeor single scattering properties at microwave and sub-millimetre wavelengths, *Earth Syst. Sci. Data* 10 (3) (2018) 1301–1326. doi:10.5194/essd-10-1301-2018.
- [18] M. Brath, R. Ekelund, P. Eriksson, O. Lemke, S. A. Buehler, Microwave and submillimeter wave scattering of oriented ice particles, *Atmos. Meas. Tech.* 13 (2020) 2309–2333. doi:10.5194/amt-13-2309-2020.
- [19] R. V. Kochanov, I. E. Gordon, L. S. Rothman, K. P. Shine, S. W. Sharpe, T. J. Johnson, T. J. Wallington, J. J. Harrison, P. F. Bernath, M. Birk, G. Wagner, K. Le Bris, I. Bravo, C. Hill, Infrared absorption cross-sections in HITRAN2016 and beyond: Expansion for climate, environment, and atmospheric applications, *J. Quant. Spectrosc. Radiat. Transfer* 230 (2019) 172–221. doi:10.1016/j.jqsrt.2019.04.001.

- [20] S. A. Buehler, M. Brath, O. Lemke, Ø. Hodnebrog, R. Pincus, P. Eriksson, I. Gordon, R. Larsson, A new halocarbon absorption model based on HITRAN cross-section data and new estimates of halocarbon instantaneous clear-sky radiative forcing, *J. Adv. Model. Earth Syst.* 14 (11) (2022). doi:10.1029/2022MS003239.
- [21] S. A. Buehler, J. Mendrok, P. Eriksson, A. Perrin, R. Larsson, O. Lemke, ARTS, the atmospheric radiative transfer simulator — version 2.2, the planetary toolbox edition, *Geosci. Model Dev.* 11 (4) (2018) 1537–1556. doi:10.5194/gmd-11-1537-2018.
- [22] M. Mech, M. Maahn, S. Kneifel, D. Ori, E. Orlandi, P. Kollias, V. Schemann, S. Crewell, PAMTRA 1.0: the Passive and Active Microwave radiative TRAnsfer tool for simulating radiometer and radar measurements of the cloudy atmosphere, *Geosci. Model Dev.* 13 (9) (2020) 4229–4251. doi:10.5194/gmd-13-4229-2020.
- [23] F. Schreier, S. G. Garcia, P. Hochstaffl, S. Staedt, Py4CAtSPYthon for Computational ATmospheric Spectroscopy, *Atmosph.* 10 (5) (2019). doi:10.3390/atmos10050262.
- [24] I. Gordon, L. Rothman, R. Hargreaves, R. Hashemi, E. Karlovets, F. Skinner, E. Conway, C. Hill, R. Kochanov, Y. Tan, P. Wcisło, A. Finenko, K. Nelson, P. Bernath, M. Birk, V. Boudon, A. Campargue, K. Chance, A. Coustenis, B. Drouin, J. Flaud, R. Gamache, J. Hodges, D. Jacquemart, E. Mlawer, A. Nikitin, V. Perevalov, M. Rotger, J. Tennyson, G. Toon, H. Tran, V. Tyuterev, E. Adkins, A. Baker, A. Barbe, E. Canè, A. Császár, A. Dudaryonok, O. Egorov, A. Fleisher, H. Fleurbaey, A. Foltynowicz, T. Furtenbacher, J. Harrison, J. Hartmann, V. Horneman, X. Huang, T. Karman, J. Karns, S. Kassi, I. Kleiner, V. Kofman, F. Kwabia-Tchana, N. Lavrentieva, T. Lee, D. Long, A. Lukashevskaya, O. Lyulin, V. Makhnev, W. Matt, S. Massie, M. Melosso, S. Mikhailenko, D. Mondelain, H. Müller, O. Naumenko, A. Perrin, O. Polyansky, E. Raddaoui, P. Raston, Z. Reed, M. Rey, C. Richard, R. Tóbiás, I. Sadiek, D. Schwenke, E. Starikova, K. Sung, F. Tamassia, S. Tashkun, J. Vander Auwera, I. Vasilenko, A. Viganin, G. Villanueva, B. Vispoel, G. Wagner, A. Yachmenev, S. Yurchenko, The hitran2020 molecular spectroscopic

- 886 database, *J. Quant. Spectrosc. Radiat. Transfer* 277 (2022) 107949.  
887 doi:10.1016/j.jqsrt.2021.107949.
- 888 [25] P. Arendas, T. Furtenbacher, A. G. Csaszar, Selecting lines for spec-  
889 troscopic (re)measurements to improve the accuracy of absolute en-  
890 ergies of rovibronic quantum states, *J. Cheminform.* 13 (1) (2021).  
891 doi:10.1186/s13321-021-00534-y.
- 892 [26] W. Wang, A. Murk, E. Sauvageat, W. Fan, C. Daetwyler, M. Hervo,  
893 A. Haefele, K. Hocke, An indoor microwave radiometer for mea-  
894 surement of tropospheric water, *IEEE T. Geosci. Remote* 61 (2023).  
895 doi:10.1109/TGRS.2023.3261067.
- 896 [27] F. Schranz, B. Tschanz, R. Ruefenacht, K. Hocke, M. Palm,  
897 N. Kaempfer, Investigation of Arctic middle-atmospheric dynamics us-  
898 ing 3 years of H<sub>2</sub>O and O-3 measurements from microwave radiome-  
899 ters at Ny-Alesund, *Atmos. Chem. Phys.* 19 (15) (2019) 9927–9947.  
900 doi:10.5194/acp-19-9927-2019.
- 901 [28] M. Lainer, K. Hocke, N. Kampfer, Long-term observation of midlat-  
902 itude quasi 2-day waves by a water vapor radiometer, *Atmos. Chem.*  
903 *Phys.* 18 (16) (2018) 12061–12074. doi:10.5194/acp-18-12061-2018.
- 904 [29] G. Mevi, G. Muscari, P. P. Bertagnolio, I. Fiorucci, G. Pace, VESPA-  
905 22: a ground-based microwave spectrometer for long-term measure-  
906 ments of polar stratospheric water vapor, *Atmos. Meas. Tech.* 11 (2)  
907 (2018) 1099–1117. doi:10.5194/amt-11-1099-2018.
- 908 [30] L. Pan, D. Lu, Terahertz band simulations using two different radia-  
909 tive transfer models, *Sci. China-Earth Sci.* 61 (10) (2018) 1482–1490.  
910 doi:10.1007/s11430-017-9242-3.
- 911 [31] E. Sauvageat, R. Albers, M. Kotiranta, K. Hocke, R. M. Gomez,  
912 G. Nedoluha, A. Murk, Comparison of Three High Resolution  
913 Real-Time Spectrometers for Microwave Ozone Profiling Instru-  
914 ments, *IEEE J. Sel. Top. Appl. Rem. Sens.* 14 (2021) 10045–10056.  
915 doi:10.1109/JSTARS.2021.3114446.
- 916 [32] F. Schranz, S. Fernandez, N. Kaempfer, M. Palm, Diurnal variation  
917 in middle- atmospheric ozone observed by ground- based microwave

- radiometry at Ny-Alesund over 1 year, *Atmos. Chem. Phys.* 18 (6) (2018) 4113–4130. doi:10.5194/acp-18-4113-2018.
- [33] L. Bernet, T. von Clarmann, S. Godin-Beekmann, G. Ancellet, E. M. Barras, R. Stubi, W. Steinbrecht, N. Kampf, K. Hocke, Ground-based ozone profiles over central Europe: incorporating anomalous observations into the analysis of stratospheric ozone trends, *Atmos. Chem. Phys.* 19 (7) (2019) 4289–4309. doi:10.5194/acp-19-4289-2019.
- [34] D. A. Newnham, M. A. Clilverd, W. D. J. Clark, M. Kosch, P. T. Verronen, A. E. E. Rogers, Ground-based Ku-band microwave observations of ozone in the polar middle atmosphere, *Atmos. Meas. Tech.* 15 (8) (2022) 2361–2376. doi:10.5194/amt-15-2361-2022.
- [35] L. Moreira, K. Hocke, N. Kaempfer, Short-term stratospheric ozone fluctuations observed by GROMOS microwave radiometer at Bern, *Earth Planets Space* 70 (2018). doi:10.1186/s40623-017-0774-4.
- [36] N. J. Ryan, M. Palm, C. G. Hoffmann, J. Goliasch, J. Notholt, Ground-based millimetre-wave measurements of middle-atmospheric carbon monoxide above Ny-Alesund (78.9 degrees N, 11.9 degrees E), *Atmos. Meas. Tech.* 12 (7) (2019) 4077–4089. doi:10.5194/amt-12-4077-2019.
- [37] Y. Shi, V. Shulga, O. Ivaniha, Y. Wang, O. Evtushevsky, G. Milinevsky, A. Klekociuk, A. Patoka, W. Han, D. Shulga, Comparison of Major Sudden Stratospheric Warming Impacts on the Mid-Latitude Mesosphere Based on Local Microwave Radiometer CO Observations in 2018 and 2019, *Rem. Sens.* 12 (23) (2020). doi:10.3390/rs12233950.
- [38] Y. Wang, V. Shulga, G. Milinevsky, A. Patoka, O. Evtushevsky, A. Klekociuk, W. Han, A. Grytsai, D. Shulga, V. Myshenko, O. Antyufeyev, Winter 2018 major sudden stratospheric warming impact on midlatitude mesosphere from microwave radiometer measurements, *Atmos. Chem. Phys.* 19 (15) (2019) 10303–10317. doi:10.5194/acp-19-10303-2019.
- [39] W. Krochin, F. Navas-Guzman, D. Kuhl, A. Murk, G. Stober, Continuous temperature soundings at the stratosphere and lower mesosphere with a ground-based radiometer considering the Zeeman effect, *Atmos. Meas. Tech.* 15 (7) (2022) 2231–2249. doi:10.5194/amt-15-2231-2022.

- [40] J. Hagen, K. Hocke, G. Stober, S. Pfreundschuh, A. Murk, N. Kaempfer, First measurements of tides in the stratosphere and lower mesosphere by ground-based Doppler microwave wind radiometry, *Atmos. Chem. Phys.* 20 (4) (2020) 2367–2386. doi:10.5194/acp-20-2367-2020.
- [41] J. Hagen, A. Murk, R. Rufenacht, S. Khaykin, A. Hauchecorne, N. Kampfer, WIRA-C: a compact 142-GHz-radiometer for continuous middle-atmospheric wind measurements, *Atmos. Meas. Tech.* 11 (9) (2018) 5007–5024. doi:10.5194/amt-11-5007-2018.
- [42] T. Lang, S. A. Buehler, M. Burgdorf, I. Hans, V. O. John, A new climate data record of upper-tropospheric humidity from microwave observations, *Sci. Data* 7 (218) (2020). doi:10.1038/s41597-020-0560-1.
- [43] M. Prange, M. Brath, S. A. Buehler, Are elevated moist layers a blind spot for hyperspectral infrared sounders? – A model study, *Atmos. Meas. Tech.* 14 (11) (2021) 7025–7044. doi:10.5194/amt-14-7025-2021.
- [44] J. He, H. Chen, Atmospheric Retrievals and Assessment for Microwave Observations from Chinese FY-3C Satellite during Hurricane Matthew, *Rem. Sens.* 11 (8) (2019). doi:10.3390/rs11080896.
- [45] F. Schreier, M. Milz, S. A. Buehler, T. von Clarmann, Intercomparison of three microwave/infrared high resolution line-by-line radiative transfer codes, *J. Quant. Spectrosc. Radiat. Transfer* 211 (2018) 64–77. doi:10.1016/j.jqsrt.2018.02.032.
- [46] O. Bobryshev, S. A. Buehler, V. O. John, M. Brath, H. Brogniez, Is there really a closure gap between 183.31 GHz satellite passive microwave and in-situ radiosonde water vapor measurements?, *IEEE T. Geosci. Remote* 56 (5) (2018) 2904–2910. doi:10.1109/TGRS.2017.2786548.
- [47] I. Moradi, M. Goldberg, M. Brath, R. Ferraro, S. A. Buehler, R. Saunders, N. Sun, Performance of radiative transfer models in the microwave region, *J. Geophys. Res.: Atm.* 125 (6) (2020) e2019JD031831. doi:10.1029/2019JD031831.

- 982 [48] R. C. Scarlat, C. Melsheimer, G. Heygster, Retrieval of total water  
983 vapour in the Arctic using microwave humidity sounders, *Atmos. Meas.*  
984 *Tech.* 11 (4) (2018) 2067–2084. doi:10.5194/amt-11-2067-2018.
- 985 [49] W. He, Z. Wang, W. Wang, Z. Zhang, Sensitivity analysis of microwave  
986 spectrometer for atmospheric temperature and humidity sounding on  
987 the new generation fengyun satellite, *IEEE J. Sel. Top. Appl. Rem.*  
988 *Sens.* 16 (2023) 853–865. doi:10.1109/JSTARS.2022.3230845.
- 989 [50] P. E. Sheese, K. A. Walker, C. D. Boone, A. E. Bourassa, D. A. Degen-  
990 stein, L. Froidevaux, C. T. McElroy, D. Murtagh, J. M. R. Iii, J. Zou,  
991 Assessment of the quality of ACE-FTS stratospheric ozone data, *At-*  
992 *mos. Meas. Tech.* 15 (5) (2022) 1233–1249. doi:10.5194/amt-15-1233-  
993 2022.
- 994 [51] H. Xu, H. Lu, Z. Wang, W. He, W. Wang, Effect Analysis of  
995 the Digital Spectrometer FFT Algorithm on THz Atmospheric Limb  
996 Sounder (TALIS) System Sensitivity, *Rem. Sens.* 13 (15) (2021).  
997 doi:10.3390/rs13152921.
- 998 [52] T. Yamada, T. O. Sato, T. Adachi, H. Winkler, K. Kuribayashi,  
999 R. Larsson, N. Yoshida, Y. Takahashi, M. Sato, A. B. Chen, R. R.  
1000 Hsu, Y. Nakano, T. Fujinawa, S. Nara, Y. Uchiyama, Y. Kasai, HO2  
1001 Generation Above Sprite-Producing Thunderstorms Derived from Low-  
1002 Noise SMILES Observation Spectra, *Geophys. Res. Lett.* 47 (3) (2020).  
1003 doi:10.1029/2019GL085529.
- 1004 [53] F. Grieco, K. Perot, D. Murtagh, P. Eriksson, B. Rydberg, M. Kiefer,  
1005 M. Garcia-Comas, A. Lambert, K. A. Walker, Improvement of  
1006 Odin/SMR water vapour and temperature measurements and valida-  
1007 tion of the obtained data sets, *Atmos. Meas. Tech.* 14 (8) (2021) 5823–  
1008 5857. doi:10.5194/amt-14-5823-2021.
- 1009 [54] W. Wang, Z. Wang, Y. Duan, Performance evaluation of THz Atmo-  
1010 spheric Limb Sounder (TALIS) of China, *Atmos. Meas. Tech.* 13 (1)  
1011 (2020) 13–38. doi:10.5194/amt-13-13-2020.
- 1012 [55] Y. Duan, Z. Wang, H. Xu, W. Wang, Simulation of the Spectrum  
1013 Response for the THz Atmosphere Limb Sounder (TALIS), *Sensors*  
1014 20 (2) (2020). doi:10.3390/s20020498.

- [56] R. Song, M. Kaufmann, M. Ern, J. Ungermann, G. Liu, M. Riese, Three-dimensional tomographic reconstruction of atmospheric gravity waves in the mesosphere and lower thermosphere (MLT), *Atmos. Meas. Tech.* 11 (5) (2018) 3161–3175. doi:10.5194/amt-11-3161-2018.
- [57] L. Li-cheng, G. Hai-yang, B. Ling-bing, Z. Qi-lin, W. Zhen, Inversion of Rotational Temperature in Airglow Layer Based on O-2 (0-1) Atmospheric Band Spectrum, *Spectrosc. Spectr. Anal.* 40 (10) (2020) 3002–3009. doi:10.3964/j.issn.1000-0593(2020)10-3002-08.
- [58] H. Gao, L. Li, L. Bu, Q. Zhang, Z. Wang, Y. Tang, Measurement of mesopause temperature using the mesospheric airglow spectrum photometer (MASP), *Opt. Communic.* 464 (2020). doi:10.1016/j.optcom.2020.125546.
- [59] S. Pfreundschuh, P. Eriksson, D. Duncan, B. Rydberg, N. Hakansson, A. Thoss, A neural network approach to estimating a posteriori distributions of Bayesian retrieval problems, *Atmos. Meas. Tech.* 11 (8) (2018) 4627–4643. doi:10.5194/amt-11-4627-2018.
- [60] I. S. Adams, S. J. Munchak, K.-S. Kuo, C. Pelissier, T. Clune, R. Kroodsmas, A. Loftus, X. Li, Active and passive radiative transfer simulations for gmp-related field campaigns, in: 2019 IEEE International Geoscience and Remote Sensing Symposium (IGARSS 2019), IEEE International Symposium on Geoscience and Remote Sensing IGARSS, Inst Elect & Elect Engineers; Inst Elect & Elect Engineers, Geoscience & Remote Sensing Soc, 2019, pp. 4553–4556, iSSN: 2153-6996.
- [61] V. Grützun, S. A. Buehler, L. Kluft, M. Brath, J. Mendrok, P. Eriksson, All-sky information content analysis for novel passive microwave instruments in the range from 23.8 GHz up to 874.4 GHz, *Atmos. Meas. Tech.* 11 (7) (2018) 4217–4237. doi:10.5194/amt-11-4217-2018.
- [62] Y. Liu, G. G. Mace, Assessing synergistic radar and radiometer capability in retrieving ice cloud microphysics based on hybrid Bayesian algorithms, *Atmos. Meas. Tech.* 15 (4) (2022) 927–944. doi:10.5194/amt-15-927-2022.

- [63] A. J. Geer, P. Bauer, K. Lonitz, V. Barlakas, P. Eriksson, J. Mendrok, A. Doherty, J. Hocking, P. Chambon, Bulk hydrometeor optical properties for microwave and sub-millimetre radiative transfer in RTTOV-SCATT v13.0, *Geosci. Model Dev.* 14 (12) (2021) 7497–7526. doi:10.5194/gmd-14-7497-2021.
- [64] S. Li, L. Liu, H. Letu, S. Hu, P. Dong, H. Ren, J. Ye, Evaluation of the impacts of ice cloud vertical inhomogeneity on spaceborne passive submillimeter-wave simulations, *Q. J. R. Meteorol. Soc.* 149 (752) (2023) 1073–1089. doi:10.1002/qj.4457.
- [65] F. Peers, P. Francis, S. J. Abel, P. A. Barrett, K. N. Bower, M. Cotterell, I. I. Crawford, N. W. Davies, C. Fox, S. Fox, J. M. Langridge, K. G. Meyer, S. E. Platnick, K. Szpek, J. M. Haywood, Observation of absorbing aerosols above clouds over the south-east Atlantic Ocean from the geostationary satellite SEVIRI - Part 2: Comparison with MODIS and aircraft measurements from the CLARIFY-2017 field campaign, *Atmos. Chem. Phys.* 21 (4) (2021) 3235–3254. doi:10.5194/acp-21-3235-2021.
- [66] M. Brath, S. Fox, P. Eriksson, R. C. Harlow, M. Burgdorf, S. A. Buehler, Retrieval of an ice water path over the ocean from ISMAR and MARSS millimeter and submillimeter brightness temperatures, *Atmos. Meas. Tech.* 11 (2018) 611–632. doi:10.5194/amt-11-611-2018.
- [67] K. D. Leppert, II, D. J. Cecil, Sensitivity of Simulated GMI Brightness Temperatures to Variations in Particle Size Distributions in a Severe Hailstorm, *J. Appl. Meteorol. Clim.* 58 (9) (2019) 1905–1930. doi:10.1175/JAMC-D-19-0031.1.
- [68] S. Pfreundschuh, P. Eriksson, S. A. Buehler, M. Brath, D. Duncan, R. Larsson, R. Ekelund, Synergistic radar and radiometer retrievals of ice hydrometeors, *Atmos. Meas. Tech.* 13 (8) (2020) 4219–4245. doi:10.5194/amt-13-4219-2020.
- [69] S. Pfreundschuh, S. Fox, P. Eriksson, D. Duncan, S. A. Buehler, M. Brath, R. Cotton, F. Ewald, Synergistic radar and sub-millimeter radiometer retrievals of ice hydrometeors in mid-latitude frontal cloud systems, *Atmos. Meas. Tech.* 15 (3) (2022) 677–699. doi:10.5194/amt-15-677-2022.



- 1081 [70] Y. Liu, G. G. Mace, Synthesizing the Vertical Structure of Tropical  
1082 Cirrus by Combining CloudSat Radar Reflectivity With In Situ Mi-  
1083 crophysical Measurements Using Bayesian Monte Carlo Integration, *J.*  
1084 *Geophys. Res.: Atm.* 125 (18) (2020). doi:10.1029/2019JD031882.
- 1085 [71] J. Gong, D. L. Wu, P. Eriksson, The first global 883 GHz cloud ice sur-  
1086 vey: IceCube Level 1 data calibration, processing and analysis, *Earth*  
1087 *Syst. Sci. Data* 13 (11) (2021) 5369–5387. doi:10.5194/essd-13-5369-  
1088 2021.
- 1089 [72] V. Barlakas, P. Eriksson, Three Dimensional Radiative Effects in Pas-  
1090 sive Millimeter/Sub-Millimeter All-sky Observations, *Rem. Sens.* 12 (3)  
1091 (2020). doi:10.3390/rs12030531.
- 1092 [73] F. Aires, C. Prigent, S. A. Buehler, P. Eriksson, M. Milz, S. Crewell,  
1093 Towards more realistic hypotheses for the information content analysis  
1094 of cloudy/precipitating situations - Application to a hyperspectral in-  
1095 strument in the microwave, *Q. J. R. Meteorol. Soc.* 145 (718, A) (2019)  
1096 1–14. doi:10.1002/qj.3315.
- 1097 [74] R. Ekelund, P. Eriksson, S. Pfreundschuh, Using passive and active  
1098 observations at microwave and sub-millimetre wavelengths to con-  
1099 strain ice particle models, *Atmos. Meas. Tech.* 13 (2) (2020) 501–520.  
1100 doi:10.5194/amt-13-501-2020.
- 1101 [75] S. Fox, J. Mendrok, P. Eriksson, R. Ekelund, S. J. O’Shea, K. N.  
1102 Bower, A. J. Baran, R. C. Harlow, J. C. Pickering, Airborne validation  
1103 of radiative transfer modelling of ice clouds at millimetre and sub-  
1104 millimetre wavelengths, *Atmos. Meas. Tech.* 12 (3) (2019) 1599–1617.  
1105 doi:10.5194/amt-12-1599-2019.
- 1106 [76] D. Casella, G. Panegrossi, P. Sano, B. Rydberg, V. Mattioli, C. Ac-  
1107 cadia, M. Papa, F. S. Marzano, M. Montopoli, Can We Use At-  
1108 mospheric Targets for Geolocating Spaceborne Millimeter-Wave Ice  
1109 Cloud Imager (ICI) Acquisitions?, *IEEE T. Geosci. Remote* 60 (2022).  
1110 doi:10.1109/TGRS.2022.3145638.
- 1111 [77] Y. Liu, S. A. Buehler, M. Brath, H. Liu, X. Dong, Ensemble opti-  
1112 mization retrieval algorithm of hydrometeor profiles for the Ice Cloud

- Imager submillimeter-wave radiometer, *J. Geophys. Res.: Atm.* 123 (9) (2018) 4594–4612. doi:10.1002/2017JD027892.
- [78] P. Eriksson, B. Rydberg, V. Mattioli, A. Thoss, C. Accadia, U. Klein, S. A. Buehler, Towards an operational Ice Cloud Imager (ICI) retrieval product, *Atmos. Meas. Tech.* 13 (2020) 53–71. doi:10.5194/amt-13-53-2020.
- [79] V. S. Galligani, D. Wang, P. B. Corrales, C. Prigent, A Parameterization of the Cloud Scattering Polarization Signal Derived From GPM Observations for Microwave Fast Radiative Transfer Models, *IEEE T. Geosci. Remote* 59 (11) (2021) 8968–8977. doi:10.1109/TGRS.2021.3049921.
- [80] J. J. Coy, A. Bell, P. Yang, D. L. Wu, Sensitivity Analyses for the Retrievals of Ice Cloud Properties From Radiometric and Polarimetric Measurements in Sub-mm/mm and Infrared Bands, *J. Geophys. Res.: Atm.* 125 (13) (2020). doi:10.1029/2019JD031422.
- [81] P. Dong, L. Liu, S. Li, S. Hu, L. Bu, Application of M5 Model Tree in Passive Remote Sensing of Thin Ice Cloud Microphysical Properties in Terahertz Region, *Rem. Sens.* 13 (13) (2021). doi:10.3390/rs13132569.
- [82] C. Weng, L. Liu, T. Gao, S. Hu, S. Li, F. Dou, J. Shang, Multi-Channel Regression Inversion Method for Passive Remote Sensing of Ice Water Path in the Terahertz Band, *Atmosph.* 10 (8) (2019). doi:10.3390/atmos10080437.
- [83] L. Liu, C. Weng, S. Li, L. Husi, S. Hu, P. Dong, Passive Remote Sensing of Ice Cloud Properties at Terahertz Wavelengths Based on Genetic Algorithm, *Rem. Sens.* 13 (4) (2021). doi:10.3390/rs13040735.
- [84] L. Shu-Lei, L. Lei, G. Tai-Chang, S. Li-Huai, Q. Shi, H. Shuai, Radiation characteristics of the selected channels for cirrus remote sensing in terahertz waveband and the influence factors for the retrieval method, *JIMW* 37 (1) (2018) 60–71. doi:10.11972/j.issn.1001-9014.2018.01.012.
- [85] H.-Y. Li, Z.-S. Wu, J.-J. Wu, L.-K. Lin, C.-S. Lu, Z.-W. Zhao, T. Qu, THz wave background radiation at upper troposphere, *Multimed. Tools and Appl.* 79 (13-14) (2020) 8767–8780. doi:10.1007/s11042-018-6803-X.

- [86] F. Cutraro, V. S. Galligani, Y. Garcia Skabar, Evaluation of synthetic satellite images computed from radiative transfer models over a region of South America using WRF and GOES-13/16 observations, *Q. J. R. Meteorol. Soc.* 147 (738) (2021) 2988–3003. doi:10.1002/qj.4111.
- [87] R. Pincus, S. A. Buehler, M. Brath, C. Crevoisier, O. Jamil, K. F. Evans, J. Manners, R. L. Menzel, E. J. Mlawer, D. Paynter, R. L. Perna, Y. Tellier, Benchmark calculations of radiative forcing by greenhouse gases, *J. Geophys. Res.: Atm.* 123 (23) (2020) e2020JD033483. doi:10.1029/2020JD033483.
- [88] S. Bourdin, L. Kluft, B. Stevens, Dependence of Climate Sensitivity on the Given Distribution of Relative Humidity, *Geophys. Res. Lett.* 48 (8) (2021). doi:10.1029/2021GL092462.
- [89] L. Kluft, S. Dacie, S. A. Buehler, H. Schmidt, B. Stevens, Re-examining the first climate models: Climate sensitivity of a modern radiative-convective equilibrium model, *J. Climate* 32 (23) (2019) 8111–8125. doi:10.1175/JCLI-D-18-0774.1.
- [90] L. Kluft, S. Dacie, M. Brath, S. A. Buehler, B. Stevens, Temperature-dependence of the clear-sky feedback in radiative-convective equilibrium, *Geophys. Res. Lett.* 48 (22) (2021). doi:10.1029/2021GL094649.
- [91] M. Gao, B. A. Franz, K. Knobelspiesse, P.-W. Zhai, V. Martins, S. Burton, B. Cairns, R. Ferrare, J. Gales, O. Hasekamp, Y. Hu, A. Ibrahim, B. McBride, A. Puthukkudy, P. J. Werdell, X. Xu, Efficient multi-angle polarimetric inversion of aerosols and ocean color powered by a deep neural network forward model, *Atmos. Meas. Tech.* 14 (6) (2021) 4083–4110. doi:10.5194/amt-14-4083-2021.
- [92] C. Emde, H. Yu, A. Kylling, M. van Roozendael, K. Stebel, B. Veihelmann, B. Mayer, Impact of 3D cloud structures on the atmospheric trace gas products from UV-Vis sounders - Part 1: Synthetic dataset for validation of trace gas retrieval algorithms, *Atmos. Meas. Tech.* 15 (5) (2022) 1587–1608. doi:10.5194/amt-15-1587-2022.
- [93] H. Yu, C. Emde, A. Kylling, B. Veihelmann, B. Mayer, K. Stebel, M. Van Roozendael, Impact of 3D cloud structures on the atmospheric trace gas products from UV-Vis sounders - Part 2: Impact on NO<sub>2</sub>

- retrieval and mitigation strategies, *Atmos. Meas. Tech.* 15 (19) (2022) 5743–5768. doi:10.5194/amt-15-5743-2022.
- [94] N. Mathew, S. Sahoo, R. R. Pillai, C. S. Raju, Millimeter-Wave Radiometric Information Content Analysis for Venus Atmospheric Constituents, *Radio Sci.* 55 (2) (2020). doi:10.1029/2019RS006913.
- [95] R. Larsson, Y. Kasai, T. Kuroda, S. Sato, T. Yamada, H. Maezawa, Y. Hasegawa, T. Nishibori, S. Nakasuka, P. Hartogh, Mars submillimeter sensor on microsatellite: sensor feasibility study, *Geosci. Instr., Methods and Data Syst.* 7 (4) (2018) 331–341. doi:10.5194/gi-7-331-2018.
- [96] D. I. Duncan, P. Eriksson, S. Pfreundschuh, An experimental 2D-Var retrieval using AMSR2, *Atmos. Meas. Tech.* 12 (12) (2019) 6341–6359. doi:10.5194/amt-12-6341-2019.
- [97] D. Ciani, M. Sabatini, B. B. Nardelli, P. L. Dekker, B. Rommen, D. S. Wetthey, C. Yang, G. L. Liberti, Sea surface temperature gradients estimation using top-of-atmosphere observations from the esa earth explorer 10 harmony mission: Preliminary studies, *Rem. Sens.* 15 (4) (2023). doi:10.3390/rs15041163.
- [98] W. Jakob, J. Rhineland, D. Moldovan, pybind11 – seamless operability between c++11 and python, <https://github.com/pybind/pybind11> (2017).
- [99] K. Schwarzschild, Ueber das gleichgewicht der sonnenatmosphäre, *Nachrichten von der Gesellschaft der Wissenschaften zu Göttingen, Mathematisch-Physikalische Klasse* 1906 (1) (1906) 41–53.
- [100] P. Baron, S. Ochiai, E. Dupuy, R. Larsson, H. Liu, N. Manago, D. Murtagh, S. Oyama, H. Sagawa, A. Saito, T. Sakazaki, M. Shiotani, M. Suzuki, Potential for the measurement of mesosphere and lower thermosphere (mlt) wind, temperature, density and geomagnetic field with superconducting submillimeter-wave limb-emission sounder 2 (smiles-2), *Atmos. Meas. Tech.* 13 (1) (2020) 219–237. doi:10.5194/amt-13-219-2020.

- [101] C. Moler, C. Van Loan, Nineteen dubious ways to compute the exponential of a matrix, twenty-five years later, *SIAM Review* 45 (1) (2003) 3–49. doi:10.1137/S00361445024180.
- [102] K. Stamnes, G. E. Thomas, J. J. Stamnes, *Radiative Transfer in the Atmosphere and Ocean* (2nd edition), Cambridge University Press, 2017, Ch. Chapter 3.3, p. 79. doi:10.1017/9781316148549.
- [103] R. Buras, T. Dowling, C. Emde, New secondary-scattering correction in disort with increased efficiency for forward scattering, *J. Quant. Spectrosc. Radiat. Transfer* 112 (12) (2011) 2028–2034.
- [104] D. Bates, Rayleigh scattering by air, *Planetary and Space Science* 32 (6) (1984) 785–790. doi:10.1016/0032-0633(84)90102-8.  
URL <http://www.sciencedirect.com/science/article/pii/0032063384901028>
- [105] J. E. Hansen, L. D. Travis, Light scattering in planetary atmospheres, *Space Science Reviews* 16 (4) (1974) 527–610. doi:10.1007/BF00168069.
- [106] R. R. Gamache, B. Vispoel, M. Rey, A. Nikitin, V. Tyuterev, O. Egorov, I. E. Gordon, V. Boudon, Total internal partition sums for the hitran2020 database, *J. Quant. Spectrosc. Radiat. Transfer* 271 (2021) 107713. doi:10.1016/j.jqsrt.2021.107713.
- [107] M. R. Zaghloul, A. N. Ali, Algorithm 916: Computing the faddeyeva and voigt functions, *ACM Trans. on Math. Softw.* 38 (2) (2012). doi:10.1145/2049673.2049679.
- [108] H. Tran, N. H. Ngo, J.-M. Hartmann, Efficient computation of some speed-dependent isolated line profiles, *J. Quant. Spectrosc. Radiat. Transfer* 129 (2013) 199–203. doi:10.1016/j.jqsrt.2013.06.015.
- [109] T. Yamada, L. Rezac, R. Larsson, P. Hartogh, N. Yoshida, Y. Kasai, Solving non-LTE problems in rotational transitions using the Gauss-Seidel method and its implementation in the Atmospheric Radiative Transfer Simulator, *A&A* 619 (2018) A181. doi:10.1051/0004-6361/201833566.

- [110] T. Karman, I. Gordon, A. van der Avoird, Y. I. Baranov, C. Boulet, B. J. Drouin, G. C. Groenenboom, M. Gustafsson, J.-M. Hartmann, R. L. Kurucz, L. S. Rothman, K. Sun, K. Sung, R. Thalman, H. Tran, E. H. Wishnow, R. Wordsworth, A. A. Vigasin, R. Volkamer, W. J. van der Zande, Update of the HITRAN collision-induced absorption section, *Icarus* (in press 2019). doi:10.1016/j.icarus.2019.02.034.
- [111] M. I. Mishchenko, L. D. Travis, A. A. Lacis, *Scattering, absorption, and emission of light by small particles*, Cambridge University Press, 2002.
- [112] G. W. Petty, W. Huang, The modified gamma size distribution applied to inhomogeneous and nonspherical particles: Key relationships and conversions, *J. Atmos. Sci.* 68 (7) (2011) 1460–1473.
- [113] S. J. Abel, I. A. Boutle, An improved representation of the raindrop size distribution for single-moment microphysics schemes, *Q. J. R. Meteorol. Soc.* 138 (669) (2012) 2151–2162.
- [114] J. Wang, X. Dong, B. Xi, A. J. Heymsfield, Investigation of liquid cloud microphysical properties of deep convective systems: 1. parameterization raindrop size distribution and its application for stratiform rain estimation, *J. Geophys. Res.: Atm.* 121 (18) (2016) 10–739.
- [115] J. S. Marshall, W. M. Palmer, The distribution of raindrops with size, *J. Meteorol.* 5 (1948) 165–166, short Contribution. doi:10.1175/1520-0469(1948)005<0165:TDORWS>2.0.CO;2.
- [116] G. M. McFarquhar, A. J. Heymsfield, Parameterization of tropical cirrus ice crystal size distributions and implications for radiative transfer: Results from cepex, *J. Atmos. Sci.* 54 (17) (1997) 2187–2200.
- [117] P. R. Field, A. J. Heymsfield, A. Bansemer, Snow size distribution parameterization for midlatitude and tropical ice clouds, *J. Atmos. Sci.* 64 (12) (2007) 4346–4365.
- [118] J. M. E. Delanoë, A. J. Heymsfield, A. Protat, A. Bansemer, R. J. Hogan, Normalized particle size distribution for remote sensing application, *J. Geophys. Res.: Atm.* 119 (7) (2014) 4204–4227.

- 1272 [119] P. R. Field, A. J. Heymsfield, A. G. Detwiler, J. M. Wilkinson, Nor-  
1273 malized hail particle size distributions from the t-28 storm-penetrating  
1274 aircraft, *J. Appl. Meteorol. Clim.* 58 (2) (2019) 231–245.
- 1275 [120] J. A. Milbrandt, M. K. Yau, A multimoment bulk microphysics param-  
1276 eterization. part i: Analysis of the role of the spectral shape parameter,  
1277 *J. Atmos. Sci.* 62 (9) (2005) 3051–3064.
- 1278 [121] I. S. Adams, J. Bobak, The Feasibility of Detecting Supercooled Liquid  
1279 With a Forward-Looking Radiometer, *IEEE J. Sel. Top. Appl. Rem.*  
1280 *Sens.* 11 (6, SI) (2018) 1932–1938, publisher: Institute of Elect & Elec-  
1281 tron Engineers Geoscience & Remote Sensing Soc; IEEE; IEEE GRSS.  
1282 doi:10.1109/JSTARS.2018.2844684.
- 1283 [122] C. F. Bohren, E. E. Clothiaux, *Fundamentals of Atmospheric Radi-*  
1284 *ation*, WILEY-VCH Verlag GmbH & Co. KGaA, 2006, ISBN 3-527-  
1285 40503-8.
- 1286 [123] K. N. Liou, *An Introduction to Atmospheric Radiation*, 2nd Edition,  
1287 Elsevier Science (USA), 2002, ISBN 0-12-451451-0.
- 1288 [124] G. E. Thomas, K. Stamnes, *Radiative Transfer in the Atmosphere and*  
1289 *Ocean*, Cambridge University Press, 1999, ISBN 0-521-89061-6.
- 1290 [125] R. M. Goody, Y. L. Yung, *Atmospheric Radiation: Theoretical Basis*,  
1291 2nd Edition, Oxford University Press, 1989, ISBN 0-19-510291-6.
- 1292 [126] I. Laszlo, K. Stamnes, W. J. Wiscombe, S.-C. Tsay, The discrete ordi-  
1293 nate algorithm, disort for radiative transfer, in: A. Kokhanovsky (Ed.),  
1294 *Light Scattering Reviews, Volume 11: Light Scattering and Radiative*  
1295 *Transfer*, Springer Berlin Heidelberg, 2016, pp. 3–65. doi:10.1007/978-  
1296 3-662-49538-4\_1.
- 1297 [127] K. F. Evans, G. L. Stephens, Microwave radiative transfer through  
1298 clouds composed of realistically shaped ice crystals. part ii. remote  
1299 sensing of ice clouds, *J. Atmos. Sci.* 52 (11) (1995) 2058–2072.
- 1300 [128] S. Fox, An evaluation of radiative transfer simulations of cloudy  
1301 scenes from a numerical weather prediction model at sub-millimetre  
1302 frequencies using airborne observations, *Rem. Sens.* 12 (17) (2020).  
1303 doi:10.3390/rs12172758.

- [129] A. Battaglia, S. Tanelli, S. Kobayashi, D. Zrnic, R. J. Hogan, C. Simmer, Multiple-scattering in radar systems: A review, *J. Quant. Spectrosc. Radiat. Transfer* 111 (6) (2010) 917–947.
- [130] T. Oguchi, N. Ishida, T. Ihara, Effect of multiple scattering on the estimation of rainfall rates using dual-wavelength radar techniques, *IEEE T. Geosci. Remote* 32 (4) (1994) 943–946. doi:10.1109/36.298023.
- [131] A. Battaglia, M. O. Ajewole, C. Simmer, Multiple scattering effects due to hydrometeors on precipitation radar systems, *Geophys. Res. Lett.* 32 (19) (2005). doi:10.1029/2005GL023810.
- [132] F. S. Marzano, L. Roberti, S. Di Michele, A. Mugnai, A. Tassa, Modeling of apparent radar reflectivity due to convective clouds at attenuating wavelengths, *Radio Sci.* 38 (1) (2003) 2–1–2–16. doi:10.1029/2002RS002613.
- [133] F. E. Roemer, S. A. Buehler, M. Brath, L. Kluft, V. O. John, Direct observation of Earth’s spectral long-wave feedback parameter, *Nature Geosci.* 16 (5) (2023) 416–421. doi:10.1038/s41561-023-01175-6.
- [134] S. Dacie, L. Kluft, H. Schmidt, B. Stevens, S. A. Buehler, P. J. Nowack, S. Dietmüller, N. L. Abraham, T. Birner, A 1D RCE study of factors affecting the tropical tropopause layer and surface climate, *J. Climate* 32 (20) (2019) 6769–6782. doi:10.1175/JCLI-D-18-0778.1.
- [135] H. He, R. J. Kramer, B. J. Soden, N. Jeevanjee, State dependence of CO<sub>2</sub> forcing and its implications for climate sensitivity, *Nature* 382 (6674) (2023) 1051–1056. doi:10.1126/science.abq6872.
- [136] P. Czarnecki, L. Polvani, R. Pincus, Sparse, empirically optimized quadrature for broadband spectral integration, *Journal of Advances in Modeling Earth Systems* 15 (10) (2023) e2023MS003819. doi:https://doi.org/10.1029/2023MS003819.
- [137] C. D. Rodgers, *Inverse methods for atmospheric sounding: theory and practice*, Vol. 2, World scientific, 2000. doi:10.1142/3171.
- [138] S. A. Buehler, P. Eriksson, O. Lemke, R. Larsson, S. Pfreundschuh, M. Brath, ARTS - The Atmospheric Radiative Transfer Simulator (2.6.0) (2024). doi:10.5281/zenodo.10813710.